EXTINCTION COEFFICIENT MEASUREMENT COMPARISON OF TUNGSTEN POWDER CLOUDS

A Thesis

presented to

the Faculty of California Polytechnic State University,

San Luis Obispo

In Partial Fulfillment

of the Requirements for the Degree

Master of Science in Mechanical Engineering

by

Spencer Grenley

September 2021

COMMITTEE MEMBERSHIP

TITLE:	EXTINCTION COEFFICIENT MEASUREMENT COMPARISON OF TUNGSTEN POWDER CLOUDS
AUTHOR:	Spencer Grenley
DATE SUBMITTED:	September 2021
COMMITTEE CHAIR:	Richard Emberley, Ph. D. Assistant Professor of Mechanical Engineering
COMMITTEE MEMBER:	Andrew Davol, Ph. D. Professor of Mechanical Engineering
COMMITTEE MEMBER:	John Ridgely, Ph. D. Professor of Mechanical Engineering

ABSTRACT

All materials in dust form pose an increased risk of accidental deflagration, or explosion. For workplace safety, this risk of deflagration for a solid particulate sample is characterized through specialized dust explosibility testing systems. These systems disperse a cloud of powder inside a spherical chamber via a pressure gradient, where a timed ignition occurs. The accuracy of measurements taken during this process are predicated upon the assumption that the cloud of powder is uniformly distributed during the ignition period. Metal additive manufacturing (AM) is a rapidly expanding technology that, in some cases, involves heavy metal powders that do not disperse well in standard explosibility testing vessels. Consequently, there is a need to validate explosibility data for heavy metal powder blends to ensure that the dust sample is adequately dispersed in the chamber at the time of ignition.

This thesis provides a method for employing optical dust probes to determine the concentration of a tungsten metal AM powder cloud inside an enclosed vessel. Optical dust probes are devices that measure light transmission through an attenuating medium, in this case a cloud of powder, and utilize Bouguer-Beer-Lambert (BBL) law to determine the concentration of particles. This thesis summarizes and synthesizes the assumptions and limitations of BBL law when used with optical dust probes, drawing from multiple published works with varying applications. The bounds of the average extinction efficiency are discussed, especially with respect to when the extinction paradox can be applied. Ultimately, it is determined that the BBL law can only be applied in this study to determine extinction coefficients, and that calculating a specific mass concentration value is theoretically misguided without specific modifications to the experimental setup. The extinction coefficients measured via an optical dust probe and a separate image analysis method are compared. Although no correlation could be established due to the limitations of this experimental setup, specific modifications are suggested that would enable this methodology to be used in future applications.

ACKNOWLEDGMENTS

I would like to begin with expressing my immense gratitude to Dr. Rick Emberley for your support, enthusiasm, guidance, and patience throughout this past year. I could not have asked for a more encouraging committee chair and mentor. I would also like to thank Dr. Andrew Davol for your constant positivity and advice, both on an academic and personal level. Thank you, Dr. John Ridgely, for your consistent comedic relief and highly technical insight, especially in the electrical realm. I will forever be grateful to the Cal Poly Mechanical Engineering department and faculty for providing all I needed during both my bachelors and masters, and for making me feel at home for the past 6 years. Lastly, thank you to Eric Pulse for your patience and time over the years – much of this experimental setup could not have been built without your help.

Thank you to the wonderful people at Lawrence Livermore National Laboratory for offering me this opportunity to learn and grow. I greatly appreciate the time and energy put forth by both Mike Ades and Matt Roberts to guide me along this process.

Thank you to my good friend, Mark Oppenheimer, for allowing me to convert his downstairs guest room into an office space during the COVID-19 shutdown so that I could get out of my small apartment. Finally, I would like to thank my friends and family for all the support and love they've given me throughout my academic career. You have always been there for me, and I could not have done this without you.

NOMENCLATURE

Variable Name	Description	Units
β	Extinction Coefficient	cm^{-1}
$\bar{\beta}$	Average Extinction Coefficient	cm^{-1}
λ	Light wavelength	nm
ρ	Material Solid Density	g / cm^3
A_P	Projected Particle Area	cm^2 / particle
C_m	Mass Concentration	g / cm^3
d_{32}	Sauter mean diameter (Vol./Surf.)	µm
d_s	Sensor Active Area Diameter	mm
d_P	Projected Particle Diameter	µm
I	Attenuated Radiant Intensity	W / m^2
I_0	Incident Radiant Intensity	W / m^2
J	Current Grayscale Pixel Intensity	8-bit unsigned integer (0 – 255)
J_0	Initial Grayscale Pixel Intensity	8-bit unsigned integer (0 – 255)
ℓ	Path Length	cm
N	Number Density	Number of particles / cm^3
Q	Extinction Efficiency	Dimensionless
$\bar{Q}$	Average Extinction Coefficient	Dimensionless
T	Measured Light Transmission	%
V	Current Voltage Reading	Volts
V_0	Initial Voltage Reading	Volts

TABLE OF CONTENTS

LIST OF TABLES

Table Page

LIST OF FIGURES

1 Introduction and Background

Additive manufacturing (AM) is a rapidly expanding technology, capable of producing complex parts that would not be possible with conventional subtractive manufacturing methods. One method of AM technology being studied is Powder Bed Fusion, a process that uses micrometer scale metal particles and sinters them layer by layer to build up a 3D part, illustrated below in Figure 1-1.

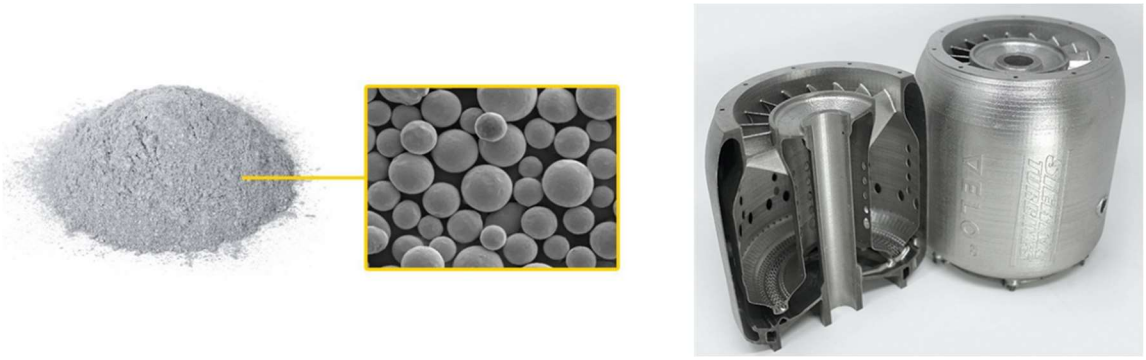

Figure 1-1. Example of metal AM powder [1] and some of the complex parts [2] that Powder Bed Fusion can produce.

Solid particulate poses a heightened risk of accidental deflagration due to its increased surface area and ability to be dispersed. If not properly handled and characterized for their explosibility risks, metal dusts can pose a potentially devastating workplace hazard[3].

Figure 1-2. Aftermath of an aluminum dust explosion that occurred in a Chinese automobile parts factory in 2014, killing 75 people and injuring 185 [4].

To prevent incidents like the aluminum dust explosion from Figure 1-2, the explosibility risk must be determined for solid particulates. Per ASTM E1226, "Standard Test Method for Explosibility of Dust Clouds", the recommended method to assess the explosibility risk of a dust sample is with a specialized testing apparatus, such as the ANKO 20L spherical test vessel seen below in Figure 1-3 [3].

Figure 1-3. The ANKO 20 Liter explosibility test apparatus is one of several devices recommended in ASTM E1226 to determine the risk of deflagration for a dust sample [5].

These dust explosibility testing systems use a pressure gradient to shoot a known mass of dust into an enclosed chamber, igniting the sample once it has been adequately dispersed. As stated in ASTM E1226, some of the key explosible parameters include the "maximum explosion pressure, P_{max}; maximum rate of pressure rise, $(dP/dt)_{max}$; and explosibility index, K_{St}". Characterizing these features for a certain dust sample is vital for developing a safety plan specific to that powder [3].

1.1 Statement of Problem

A key assumption made when performing explosibility testing with systems like the ANKO 20L spherical vessel is that the powder sample is adequately dispersed inside the chamber at the time of ignition. Systems like the ANKO 20L are designed to reliably suspend lighter weight dust samples during the timed ignition period, accommodating the majority of solid particulate seen in industry. However, researchers at Lawrence Livermore National Laboratory (LLNL) have found that some heavier metal AM powders, such as tungsten, do not disperse properly inside the ANKO 20L vessel during testing. Modifications to the explosibility testing apparatus must be made to accommodate these heavier powders, specifically with the nozzle that disperses the pressurized blast of dust. To validate explosibility data from a modified testing vessel, there is a need to develop a method(s) to quantitatively evaluate dust presence and cloud uniformity over time inside the chamber.

1.2 Previous Work

Before this project, engineers at LLNL produced a transparent replica of the ANKO 20L vessel to acquire highspeed footage of powder clouds produced by their various nozzle redesigns. This system, shown in Figure 1-4, incorporated plastic FDM components, a transparent acrylic globe, and a transparent vacuum chamber. The powder cloud was injected via the same ANKO fast-acting valve (FAV) system from the original ANKO 20L spherical apparatus.

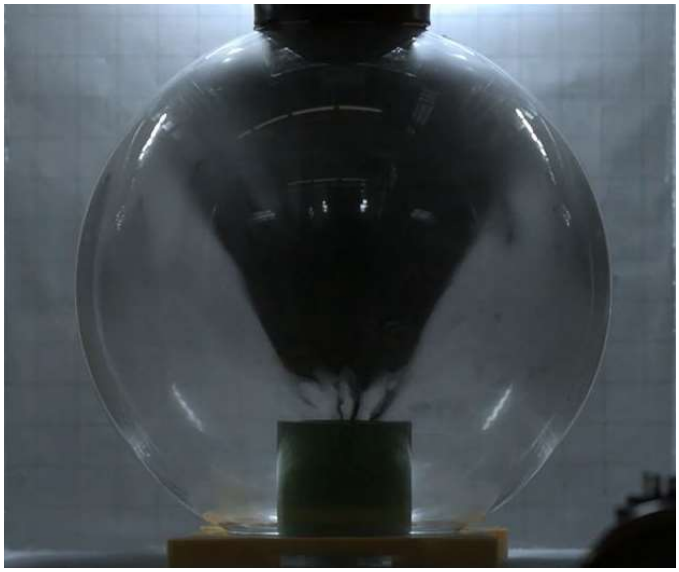

Figure 1-4. Transparent replica of ANKO 20L spherical apparatus for highspeed filming of the cloud.

The development of the transparent globe inspired another Cal Poly thesis, which was completed by Shelby Lampshire. This thesis, "Metal Dust Cloud Distribution Characterization Through Image Analysis", worked to analyze highspeed footage in MATLAB and provide a quantitative assessment of cloud uniformity, both spatially and temporally. Lampshire's project was worked on in parallel to this thesis, with mostly the same test setup at Cal Poly. Aspects of Lampshire's work were both referenced and adapted into this thesis [6].

1.3 Objective

The first objective of this thesis was to research and develop a metrology solution that measures dust presence, ideally in the form of a mass concentration (g/cm^3), over time inside of the ANKO 20L vessel. Some of the important design parameters were that the system could not directly interfere with the powder cloud, could provide a continuous measurement, and could be implemented into the ANKO vessel. These requirements limited the options to optical particulate counters. The second and final objective was to compare data collected from this metrology solution to radial trace data (described in section 3.2.2.2) generated by Lampshire's image analysis method.

2 Literature Review

2.1 Optical Dust Probes

The primary source that both inspired and informed this thesis was the "Three Bureau of Mines Optical Dust Probes" study, published in 1981 by researchers from Pittsburgh Research Laboratory (PRL) [7]. This report, which will be referred to simply as the "Three Probes study" throughout this paper, detailed the design and application of optical dust probes for measuring the mass concentration of a dust cloud inside an enclosed chamber. Specifically, these probes were designed for the U.S. Bureau of Mines to measure dust clouds produced inside a Siwek 20L explosibility testing apparatus, which is very similar in both form and function to the ANKO 20L vessel acquired by LLNL [8]. The Three Probes study provided a thorough explanation of the theoretical limitations of these probes, as well as the rigorous calibration process required to calculate a mass concentration value with them. Within the context of this thesis, an *optical dust probe* refers to a device that measures the light transmission through an attenuating medium (in this case, a cloud of particles). A basic schematic of this is illustrated below in Figure 2-1.

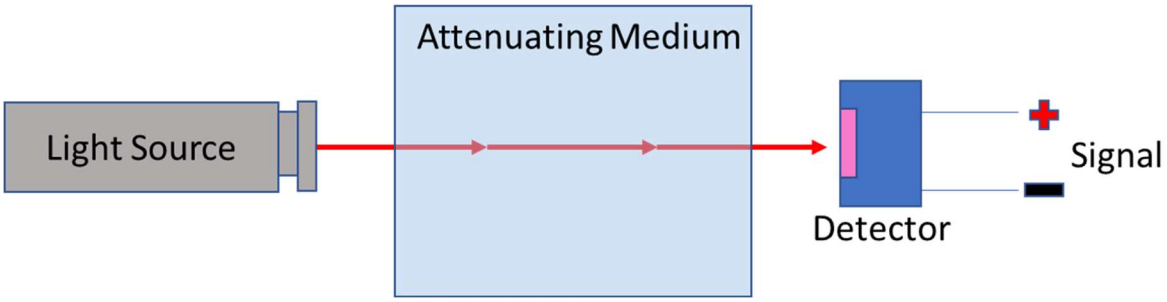

Figure 2-1. Illustration of an optical dust probe, a device that measures light transmission through an attenuating medium. The probe consists of a paired light source and photodetector.

With the appropriate experimental setup, this measured light transmission can be used to ultimately calculate a mass concentration value over time for a dust cloud using Bouguer-Beer-Lambert Law (discussed in detail in section 2.3). Although this thesis focuses on transmission-based probes, it is important to acknowledge that a separate style of optical particulate counters (OPC's) exist that measure scattered light instead of transmitted light. Some of these OPC's include:

- Raman probes that operate on the principle of Raman inelastic backscattering [9]
- Snow Particle Counters (SPC's) that utilize Fraunhofer diffraction theory [10]
- Photometers that utilize Mie scattering theory [11]

While these technologies could potentially have worked well, transmission-based optical dust probes had already been shown to be successful in this specific application. Considering the short timeline of this thesis, transmission-based probes were ultimately pursued over the diffraction-based OPC options.

2.2 Particle-Light Interaction

Light is defined as the relatively small band of visible wavelengths within the electromagnetic radiation spectrum [12]. Although most of the phenomena involved with light can be described with wave-physics, some phenomena, such as the photoelectric effect with a photodiode, suggest that light can also be treated as a stream of individual particles. Consequently, a duality exists for light in that, for some observable and quantifiable phenomena, it should be treated as a wave, while in others, as a stream of massless particles called photons [13]. This section and the following theoretical discussion involving the interaction of light with a spherical particle will lean on the wave description of light. Furthermore, with nanoscale wavelengths, each light wave can be approximated as a ray. Consider a single spherical particle interacting with perfectly collimated rays of incident EM radiation, illustrated in Figure 2-2.

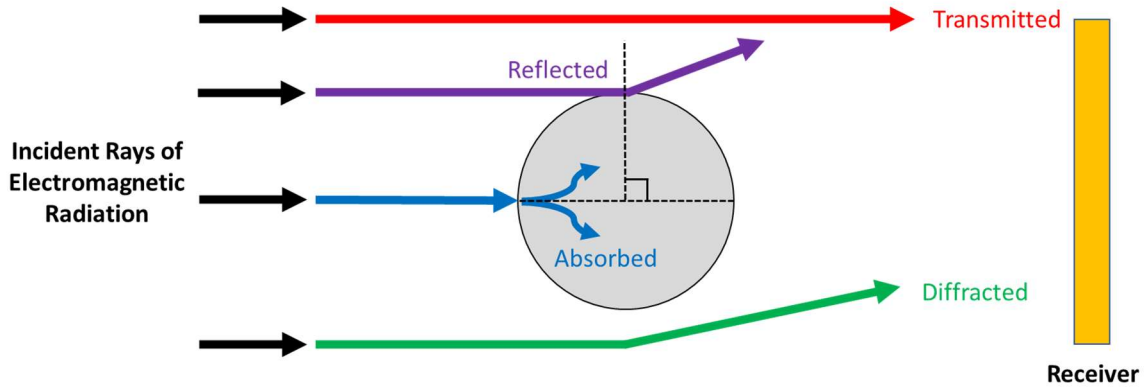

Figure 2-2. Illustration of a spherical particle interacting with perfectly collimated incident electromagnetic radiation. Only the four relevant types of light interactions are depicted: transmitted, reflected, absorbed, and diffracted light.

While Figure 2-2 illustrates the relevant manners that light is expected to interact with a metal AM particle, the schematic is by no means an exhaustive list of how light could interact with any given particle. In this instance, *transmitted light* describes the rays of light that the particle does not interact with. *Forward scattered light* is any light that is diffracted or reflected by the particle that travels beyond the forward plane (illustrated in Figure 2-2 by the line perpendicular to the collimated incident rays) [12].

Diffraction is a particularly interesting light interaction and describes the tendency of light rays to both interfere with one another and to bend around an object as they pass its outer edges. This phenomenon is responsible, in part, for the shape and size of shadows cast by objects, specifically for the darker area known as the *shadow region*, illustrated below in Figure 2-3 [14].

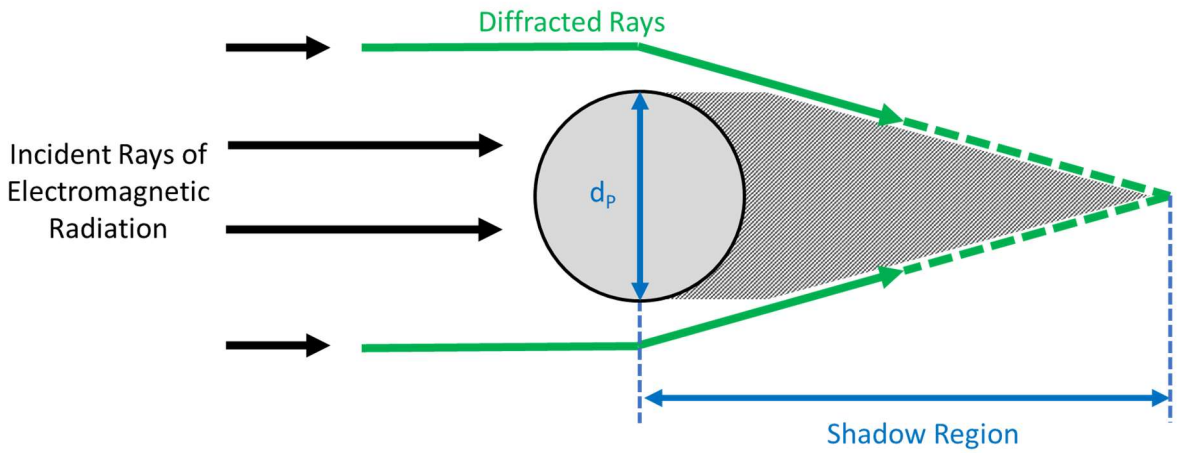

Figure 2-3. An illustration of the shadow region of a spherical particle.

The length of a shadow region describes the distance away from an object that light is still obstructed. The value of this distance can be approximated by the following equation:

$$\text{Length of Shadow Region} \approx \frac{10{d_P}^2}{\lambda} \qquad \text{Eqn. (1)}$$

The importance of a particle's shadow region will be expanded upon in section 2.5.1.

2.3 Bouguer-Beer-Lambert Law

Bouguer-Beer-Lambert law (BBL law for short) is one of the most important equations in the realm of optical metrology. This law can be used to relate the light transmitted through a certain length of an attenuating medium to the concentration of that medium. Its equation form is expressed below:

$$T = \frac{I}{I_0} = \exp(-\beta \ell) \qquad \text{Eqn. (2)}$$

Theoretically, *Path length*, ℓ, is the distance that the light being measured travels through the attenuating medium. This is an important distinction to make, as it is not simply the distance between the light source and detector if the attenuating medium does not fully occupy the space between them. When applied to a dust cloud, this parameter assumes a uniform distribution of powder [12]. Some concerns with this concept are discussed in Section 5.1.2.

Another key variable is the *extinction coefficient*, β, with units of cm^{-1}. Physically, the extinction coefficient represents how much light intensity is obscured for each centimeter the light travels through the attenuating medium [12]. Referencing a uniform cloud of particles, the extinction coefficient can be broken down into the following equation:

$$\beta = NA_P Q \qquad \text{Eqn. (3)}$$

The *number density*, N, represents the number of particles in the volume actively attenuating the light source. For instance, if a perfectly collimated laser beam is the light source, the number density represents the amount of uniformly distributed particles that fall inside the cylindrical column of the beam [15].

Perhaps the most important variable contained in Eqn. (3) is the dimensionless *extinction efficiency*, Q. It is important that the extinction efficiency is not confused with the extinction coefficient, β. The efficiency is dimensionless, and describes an individual particle, whereas the extinction coefficient has units of cm^{-1} and describes the cloud of those particles. Specifically, the extinction efficiency represents how effective a single particle is at blocking light from reaching the detector, and can be represented by the following expression given by Ogle [15]:

$$Q = \frac{Radiant\ Power\ absorbed\ and\ scattered\ by\ particle}{Radiant\ Power\ geometrically\ incident\ to\ particle} \qquad \text{Eqn. (4)}$$

The extinction efficiency is based on complex Mie Scattering Theory, which solves Maxwell's equations for specific light interaction cases. A discussion on characterizing the extinction efficiency for a given cloud is presented in section 2.5.

2.4 Theoretical Assumptions

Many of the key theoretical assumptions and limitations of Bouguer-Beer-Lambert law are very restrictive and, unless modified, would prevent this law from being applied to most real-world situations. One of the first modifications to BBL Law stems from recognizing that a monodisperse cloud will not likely exist in an experimental setting, especially one involving a dynamic cloud of particles. The term *monodisperse* describes a cloud of particles with uniform size and mass. Even with precision metal AM powders that likely have a more consistent diameter relative to other dust samples, agglomeration effects can alter the effective diameters of particles. *Agglomeration* is the tendency of particles to clump together in a reversible and sometimes temporary manner. This randomized clumping of particles can alter the effective diameters of particles within the powder cloud, leading the cloud to become polydisperse. The degree of agglomeration occurring is described by the *agglomeration factor*, α, which is a multiplier that implies how much the particle size has increased. A value of $\alpha = 1$ means that no agglomeration occurred. The way to account for this is to simply switch the extinction coefficient equation in Eqn. (3) to averages, thus allowing it to be used in polydisperse clouds [7]. This can be seen below:

$$\bar{\beta} = N\bar{A}_P\bar{Q} \qquad \text{Eqn. (5)}$$

Once this step has been taken, the following table summarizes the main assumptions made in applying BBL Law to this experiment. If no modification was made, that implies that the experimental setup met that theoretical assumption.

Table 2-1. List of the main theoretical assumptions, as well as modifications to those assumptions if necessary. Note that this is not an exhaustive list of all possible assumptions.

#	Theoretical Assumption	Modification	Reference
1	Homogeneous cloud	--	[12]
2	Monodisperse cloud	Polydisperse is okay	[7]
3	High sphericity	--	[12] [15]
4	Low concentration of particles	Particles just need to be spaced a few particle diameters away from each other and have minimal EM interactions	[7]
5	Uniformly distributed cloud	Non-uniform okay *	[7]
6	Monochromatic light source	Polychromatic/white light okay **	[16] [15]
7	Perfectly collimated light source	Okay for not collimated **	[16] [15]
8	Ambient pressure and temperature	Pressurized clouds are okay	[7]
9	Constant/known sensor response	--	[7]
* The implications of a highly nonuniform cloud will be discussed in Section 5.1.2 ** Collimated and monochromatic light sources are preferable – discussed in section 2.5.2			

One of the key assumptions made when dealing with any light-particle interactions is a high degree of *sphericity*, which is the measure of how closely a particle can be approximated as a sphere. This is generally a poor assumption to make in cases involving dust samples, as most particles possess a low degree of sphericity. However, as shown in Figure 2-4, metal AM powders are unique in that they possess some of the highest sphericity possible in the realm of solid particulate, as this is a critical feature for their use in additive manufacturing [17].

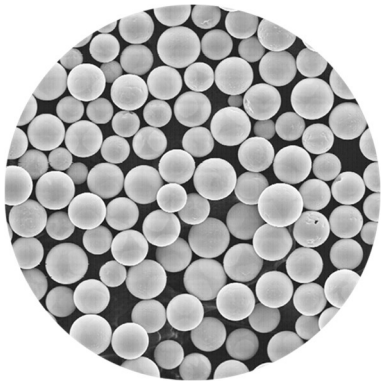

Figure 2-4. Image of TEKNA additive manufacturing metal powder, showcasing the high sphericity of precision AM metal powders [17].

2.5 Mass Concentration from BBL Law

The process of calculating a mass concentration from BBL Law is difficult and doing so requires a carefully constructed experimental setup. BBL Law can be rewritten in the following form to solve for the concentration, involving a substitution predicated on the assumption of high particle sphericity:

$$C_m = \frac{2\rho d_{32}}{3\bar{Q}\ell} * \ln(T) \qquad \text{Eqn. (6)}$$

The key to calculating a mass concentration value in g/cm^3 from BBL Law using Eqn. (6) is to characterize both:

1) The average extinction efficiency of the cloud at that moment in time
2) The Sauter mean diameter, acknowledging that particles may agglomerate

Characterizing the diameter of particles can be done in many ways; however, agglomeration effects should be considered as they can be process dependent. For instance, one common method for determining particle size distribution is via a Coulter Counter device. This process involves dispersing the dust sample in isopropyl alcohol, which breaks up any agglomeration effects [7]. If used as the sole metric, this could produce misleading results that would likely be inconsistent with the particle size distribution in the cloud. An example of a system that would work quite well in determining the agglomeration factor in this

application would be a particle size distribution (PSD) analyzer such as the TSI model EEPS 3090. This PSD analyzer has been successfully used to characterize the agglomeration of nanoscale aluminum AM powder being dispersed inside a 20L dust explosibility apparatus. The EEPS 3090 can measure the size distribution of particles suspended in the air in real time, thus determining the transient agglomeration factor for particles in a cloud [18].

2.5.1 The Extinction Paradox

As mentioned previously, the extinction efficiency, Q, of a particle is based on complex Mie Scattering Theory. From this theory, a useful asymptotic relationship exists for the extinction efficiency of a particle under the following conditions:

$$Q \rightarrow 2 \text{ for when } \lambda \ll \pi d_P \ \& \ d_P > 4\mu m \qquad \text{Eqn. (7)}$$

This phenomenon is called the *extinction paradox*. So long as conditions listed in Eqn. (7) are met, a particle can only remove twice as much light from reaching the detector than it would do so with its projected area, regardless of the particle's size. This occurs through a combination of scattering, diffraction, and absorption of the incident light [12] [15].

An important stipulation of this that Hinds [12] discusses is that the sensor must be sufficiently removed from the shadow region of a particle so that the forward scattered light does not reach the sensor's active area. This distinguishes the extinction efficiency as less of an inherent property of the particle, but as a value that describes the interaction between that particle and the detector.

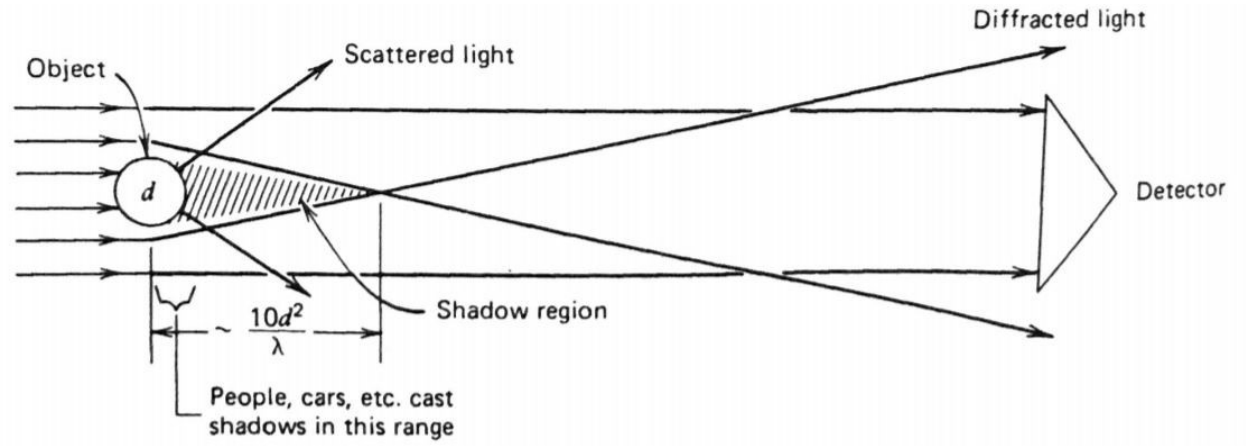

Figure 2-5. A diagram from Hind's textbook, *Aerosol Technology*, illustrating the extinction paradox [12].

Extrapolating on this information and Hind's schematic, shown in Figure 2-5, a rough calculation was performed to approximate the distance a detector needs to be away from the particle it is measuring to avoid detecting forward scattered light. This approximation is based on a simplified model shown below in Figure 2-6.

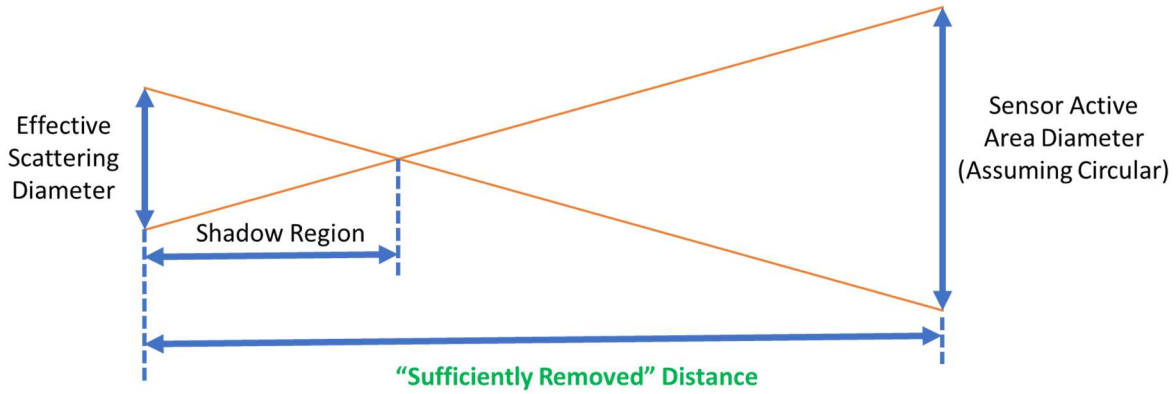

Figure 2-6. Extrapolation of the extinction paradox diagram from Hind's text to approximate the distance a sensor needs to be from a particle for no forward scattered light to reach it.

If the particle is indeed removing twice as much light as it would with just its geometry, an *effective scattering diameter* (a term contrived for this discussion) would exist from doubling the geometric area of the particle. This is likely an oversimplification of what is occurring due to the complexity of light

interactions, but is an educated guess given the information available. Using basic trigonometry with similar triangles, an approximation of the "sufficiently removed" distance could be described as:

$$\text{Sufficient Distance} \approx \frac{10{d_P}^2 + 5\sqrt{2}\, d_P\, d_S}{\lambda} \qquad \text{Eqn. (8)}$$

A more conservative approximation for the sufficiently removed distance would simply use the particle diameter in the trigonometry instead of an effective scattering diameter:

$$\text{Conservative Sufficient Distance} \approx \frac{10{d_P}^2}{\lambda}\left(1 + \frac{d_S}{d_P}\right) \qquad \text{Eqn. (9)}$$

The value from Eqn. (9) was found to be about 1.4 times greater than the distance from Eqn. (8) with the inputs from this experiment (detailed in later sections) and is likely overly conservative. The set of calculations for Eqn. (8) and Eqn. (9) can be seen in appendix A.9.

The application of the extinction paradox on a global level for a cloud is justified for atmospheric measurements, where the sensor is a significant distance away from most of the aerosolized particles. Furthermore, atmospheric applications allow for a looser interpretation of BBL law assumptions and agglomeration effects can potentially be ignored. This was displayed in a novel report by Purdue University researchers, where BBL law was applied in an atmospheric measurement setting to find the extinction coefficient over time of an aerosolized particulate using iPhone 7 cameras (specifically their CCD sensors). Despite later acknowledging that the particles within the cloud were agglomerating, the researchers stated that the cloud was assumed to be monodisperse. Additionally, the light source utilized was polychromatic ambient lighting. The researchers compared their results to a calibrated laser probe and found that the datasets closely aligned, to the extent that their measured extinction coefficient directly correlated to a verified mass concentration of a given cloud [16].

2.5.2 Sensor Proximity to Dust Cloud

Unfortunately, when using optical dust probes to measure the transmitted light inside of a vessel, the extinction paradox cannot be applied as easily as it can in longer range applications. Due to the proximity of the sensor and the particles, some of the scattered light will likely reach the detector's active area. In thorough experimentation completed by PRL scientists in the Three Probes study, the bounds of $\overline{Q}$ when the sensor is in proximity to the cloud is [7] :

$$1 \leq \overline{Q} \leq 2$$

The lower bound extinction efficiency of $\overline{Q} = 1$ means that the sensor sees all the scattered light, and that the particles are only blocking the light incident to them geometrically. The upper bound extinction efficiency of $\overline{Q} = 2$, the extinction paradox, means that none of that scattered light is reaching the detector. In this upper bound case, the only light measured by the detector is transmitting through without interacting with the particles, and all scattered light is blocked [7].

When the sensor is in proximity to the particles, there are two methods that allow for the characterization of the extinction efficiency:

1) Physically blocking the scattered light with precision optical devices [12]
2) Thorough calibration process with a known quantity of dust [7]

Physically blocking the scattered light from reaching the detector is certainly the least time-consuming manner to characterize the extinction efficiency, as it allows for the extinction paradox of $\overline{Q} = 2$ to be applied. This method, depicted in Figure 2-7, requires a precise experimental design involving a well-collimated light source, lenses, and pin hole apertures to narrow the sensors field of view.

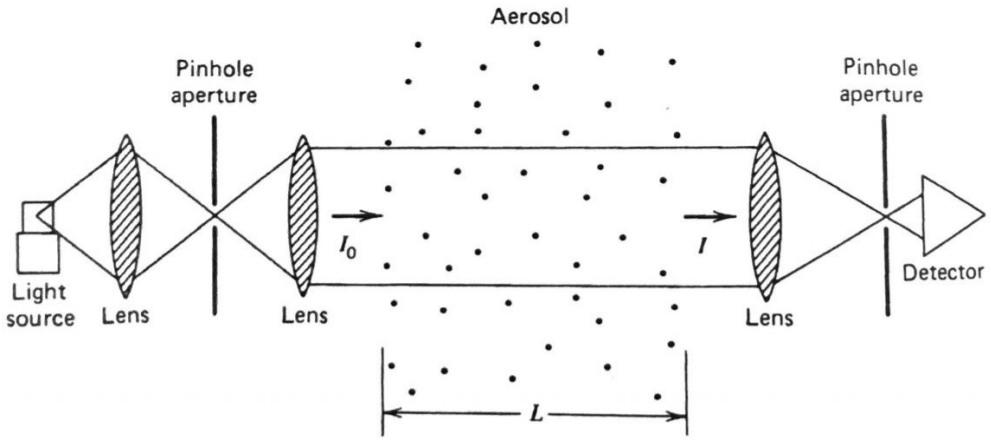

Figure 2-7. A probe setup that physically blocks scattered light from reaching the detector. For particles with a diameter substantially greater than the wavelength of the incident light, the extinction paradox would hold true [12].

Using precision lasers as the light source was shown to be a very important design feature in the Three Probes report. In the study, LED light sources were used and, although the researchers took extensive measures to limit the field of view of their detector and collimate the light, they found that a large amount of non-parallel rays were still detected. In their calibration process, they verified this by testing their setup against a Helium-Neon laser, which they stated as reliably having an extinction efficiency of $\overline{Q} = 2$. Presumably, the reason they used LEDs in their probe design was that this paper was published in 1981. Although the first semi-conductor laser diode was developed in the early 60's, it was not until the end of the 20th century that these modules had advanced to reliably operate at room temperature in the compact form that exists today. The probes that the PRL researchers were designing required the light source to have a relatively small footprint, which likely ruled out the usage of large and potentially fragile gas-based lasers [19]. Today, laser semi-conductor diodes are reliable and compact. They produce a beam of coherent, directional, and highly monochromatic light that is far easier to collimate than the incoherent, nondirectional, polychromatic light emitted by an LED [20].

The caveat to this setup is that the agglomerated particle diameter still must be determined for a mass concentration value to be successfully backed out of BBL Law. This likely would necessitate some

calibration to understand the degree of agglomeration occurring within the powder cloud, as this is dependent on the method of cloud dispersion, powder material, and other environmental factors.

When the probe setup cannot produce a well-collimated beam nor block forward scattered light from reaching the detector, the next solution to calculating a mass concentration value is through extensive calibration. This, ultimately, is what the PRL researchers had to do to in their Three Probes study. Their first attempt at calibration was to create stationary dust clouds by encapsulating various amounts of powder in clear epoxy, shown below in Figure 2-8.

Figure 2-8. Epoxy samples experimented with for probe calibration in the Three Probes study [7].

The main shortcoming of this method was that the particles contained in the plastic sample were deagglomerated when mixed with the epoxy and failed to accurately represent the size distribution seen in a dust cloud. Recognizing the need to simulate the cloud dispersal method that the probes would ultimately be used with, a smaller pressurized vessel was acquired for calibration.

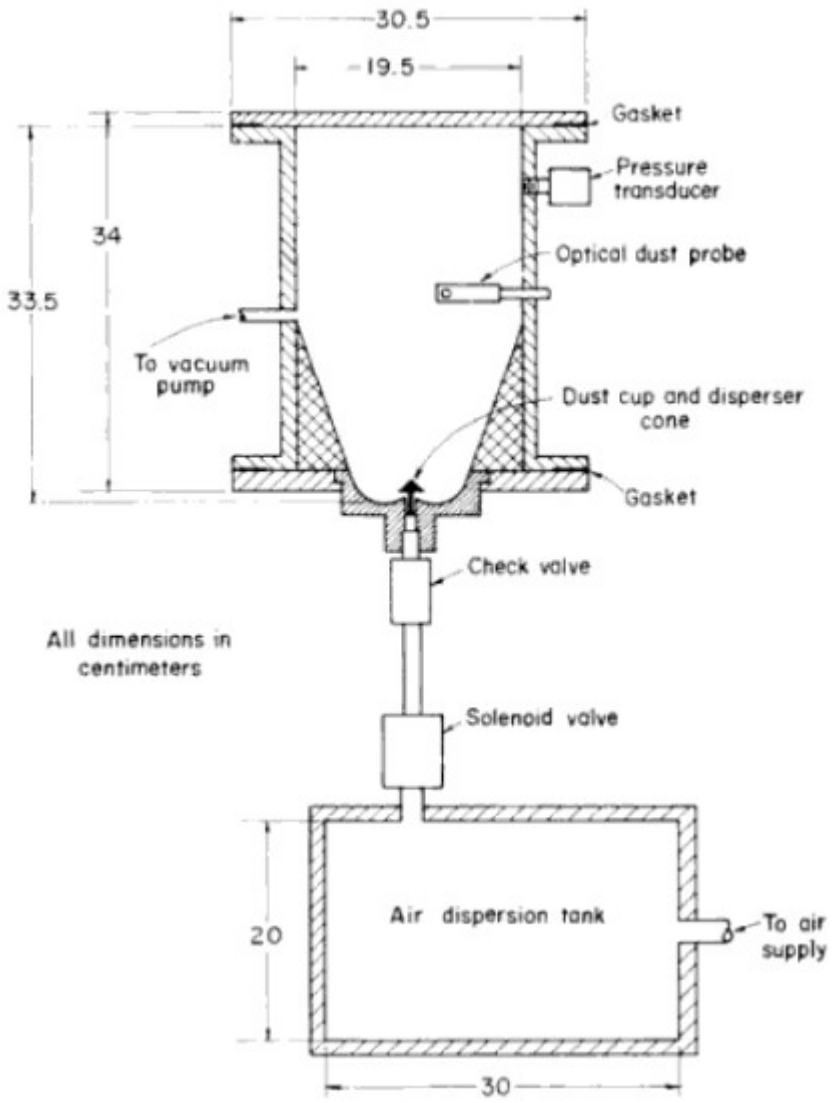

Figure 2-9. Pressurized calibration vessel from PRL's Three Probes study. This vessel allowed for a known quantity of powder to disperse uniformly into a known volume, mirroring any agglomeration effects that occurred in the dust explosibility chamber.

This cylindrical calibration vessel acquired by PRL researchers, shown above in Figure 2-9, enabled them to uniformly disperse a specific quantity of powder into a known volume. The vessel also possessed a clear viewing window at the top of the chamber so that the uniformity of the cloud could be visually confirmed via highspeed footage. Any agglomeration effects that occurred in the Siwek 20L spherical apparatus would likely be mirrored in this setup.

Instead of separately finding the average extinction efficiency, $\overline{Q}$, and the Sauter mean diameter, d_{32}, they lumped the two unknown parameters together (along with the known solid density) to form the term $\rho\, d_{32}/\overline{Q}$. Effectively, they were able to predetermine the mass concentration that would occur in the powder cloud, and then rearrange Eqn. (6) to empirically solve for $\rho\, d_{32}/\overline{Q}$:

$$\frac{\rho d_{32}}{\overline{Q}} = \frac{3C_m \ell}{2 \ln (T)} \qquad \text{Eqn. (10)}$$

To determine the degree of agglomeration occurring in the cloud, the mean deagglomerated diameter was found using a Coulter Counter size analysis, where a sample of dust was dispersed in isopropyl alcohol. Agglomeration was prevented through this mixing and dispersal in alcohol, and therefore, provided a deagglomerated diameter to compare with to the experimentally determined d_{32} (measured via a precision laser light source with a known extinction coefficient). Through this process, they confirmed that many of the powders they tested were, indeed, experiencing a significant degree of agglomeration in the cloud. Additionally, the researchers were able to calibrate their LED probes to backout a reliable mass concentration for each type of powder [7].

3 Methodology

3.1 Experimental Setup and Design

The key features of the experimental setup used in this thesis were the containment vessel, powder dispersion method, dust material, highspeed camera/backlight, optical dust probe/mounting solution, and DAQ/control. Several of these components can be seen in Figure 3-1.

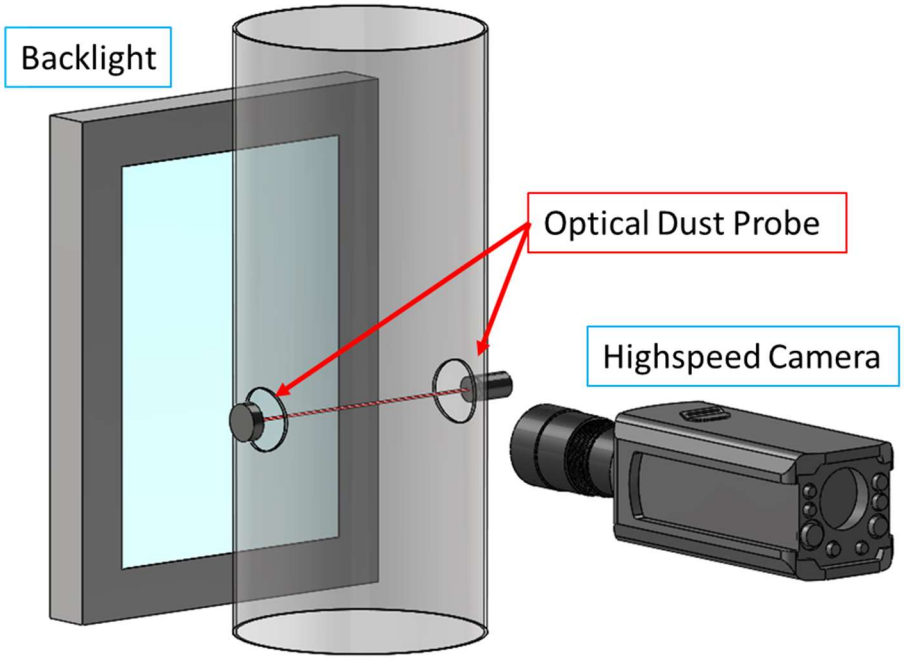

Figure 3-1. A model showing the relative positioning of several key features in the experimental setup. These key features include the transparent containment vessel, highspeed camera, backlight, and optical dust probe.

3.1.1 Containment Vessel

An acrylic cylinder with an inner and outer diameter of 9.75” and 10”, respectively, was used as the transparent containment vessel. To provide a clear line of sight for the probe, two diametrically positioned holes were drilled into the cylinder using a 2.5” hole saw. These holes were effectively plugged by the 3D printed probe mounting assemblies, which will be discussed later. The top of the cylinder was sealed with a rubber ring and an acrylic disc, which were both laser cut. At the sides, the cylinder was fixed

to a 40mm T-slot frame and raised off the surface of the table. A powder collection pan was then pressed up against the bottom of the cylinder and secured in place to catch the falling powder. A rubber ring kept the powder inside the cylinder until the pan was released and removed to recollect the powder.

3.1.2 Powder Dispersion Method

Within the sealed containment vessel, a system was designed to produce a cloud of dust for each trial. The main criteria for the powder dispersion method were that it needed to:

1. Deliver a known mass of powder all at once,
2. Enable timed triggering from LabVIEW,
3. Not involve any pressurized components,
4. Produce an axisymmetric or, even better, homogeneous dust cloud.

The restriction of not being able to utilize pressurized components due to safety concerns limited the viable designs options. The chosen design concept drew inspiration from a project done by a YouTube engineer, Mark Rober, where he designed a contraption that ejected glitter from a spinning dish using centripetal acceleration [21]. The glitter bomb design from Rober's project can be seen in Figure 3-2 below.

Figure 3-2. The inspiration behind the dust dispersion system - Mark Rober's glitter bomb [21].

The dust dispersion method used in this project consisted of a highspeed 12VDC brushed hobby motor that rapidly spun a 3D printed powder bowl, ejecting the powder contained within it via centripetal acceleration. This powder then rebounded off the inside of a stationary deflector shield that surrounded the spinning bowl, causing the powder to redirect downwards in a more dispersed and centralized manner.

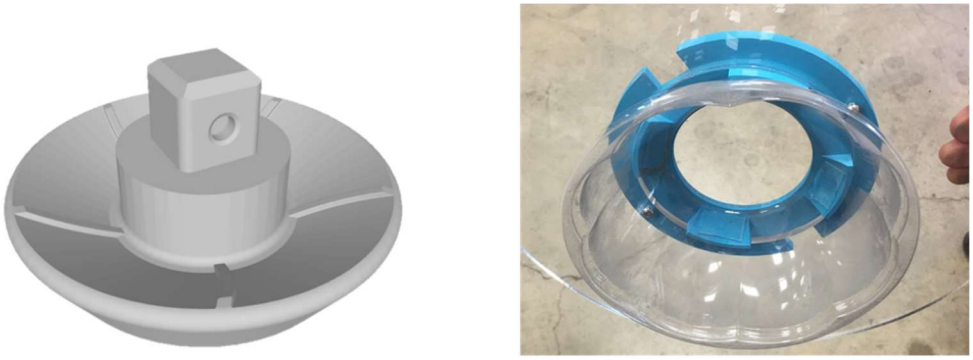

Figure 3-3. Main components of powder dispersion method: the spinning powder bowl and deflector shield.

As shown above in

Figure 3-3, the spinning powder bowl had ribs along the inside surface to help push powder out. The square peg protruding from the center of the bowl was fixed to a separate 3D printed assembly, locking it to the rotating motor shaft. The deflector shield, pictured on the right in

Figure 3-3, was chosen for its shape, transparency, and availability. The shield was adhered to a 3D printed adapter ring using double-sided 3M VHB tape. The 12 VDC motor was controlled by a X-NUCLEO-IHM04A1 motor driver. The full assembly can be seen below in Figure 3-4.

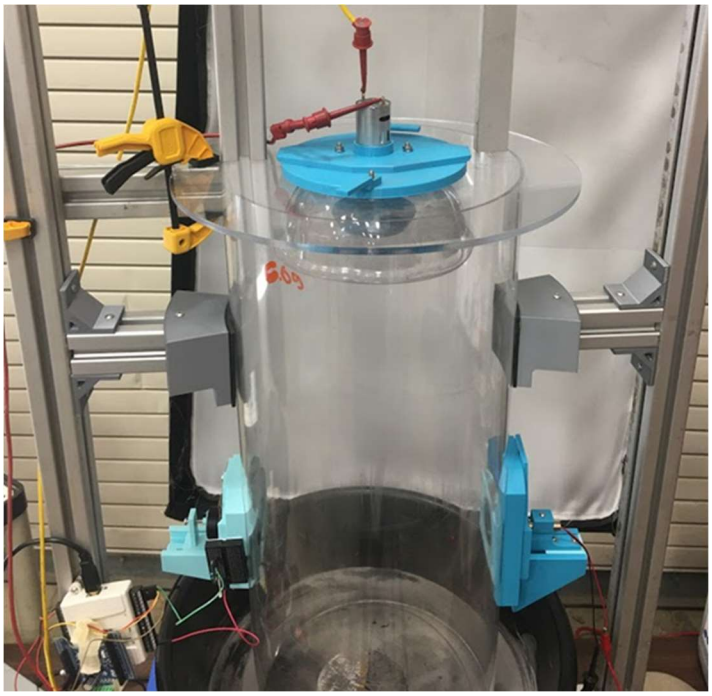

Figure 3-4. Full dust dispersion assembly, as used in situ.

The laser cut acrylic top lid of the enclosure containing the dust dispersion assembly had to be fixed using extra T-slot and trigger clamps. Snapshots of the dust being ejected from the system and falling to the bottom of the vessel can be seen below in Figure 3-5.

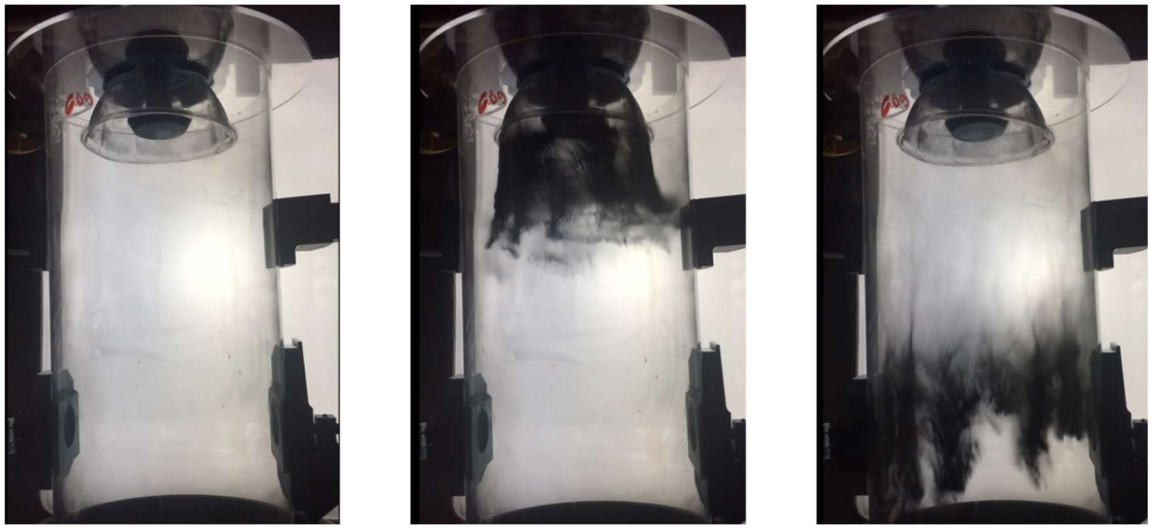

Figure 3-5. Snapshots of the powder cloud forming in the vessel. The powder was ejected from the dust dispersion system and then fell to the bottom collection pan.

As seen above in Figure 3-5, the dust dispersion method released the powder cloud when triggered. The powder did tend to clump together and form plumes, so the uniformity goal of the cloud was not met. More on this will be discussed in section 4.1.1. Overall, given the limited time and resources, this dust dispersion method adequately met the demands bounded by the scope of this study.

3.1.3 Material

The material utilized in this paper was TEKNA W-45 tungsten AM powder. The average diameter was determined to be approximately 28 μm via a particle size distribution (PSD) analysis by LLNL. Regarding safety, this powder had previously been characterized by LLNL as having low general handling risks and low explosibility. The particle density of the powder was also provided by LLNL documentation to be 19.3 g/cm^3. This information is summarized in Table 3-1.

Table 3-1. Characteristics of TEKNA W-45, tungsten AM powder

Characteristic	Value
Explosibility Risk	Low
General Handling Risks	Low
Average Particle Diameter	28 μm
Sphericity	High
Particle Density	19.3 g/cm3

Figure 3-6. Weighing out 40g of tungsten powder for each sample.

During each trial, 40g of this powder was measured out directly into the bowl on an OHAUS scale, as seen above in Figure 3-6. After the powder was added, an effort was made to tap the bowl such that the powder was distributed evenly across it, although it should be noted that minor variations likely occurred between trials.

3.1.4 Highspeed Camera and Backlight

The highspeed camera utilized in this experiment was a Phantom v310. The backlight used was a 150-Watt fluorescent light in a soft box. The camera was controlled via Phantom software on a dedicated PC. This setup can be seen in Figure 3-7.

Figure 3-7. Phantom highspeed camera setup.

The camera filmed in grayscale using a Sigma macro lens. When filming, the room lights were turned off and the windows were blocked to minimize ambient light. During the initial setup of the camera and lights, a strobe effect with the AC powered backlight was observed when filming at higher frame rates. This was determined to be the result of the AC current frequency from the wall outlet. When footage was taken at 120 fps to match the 120 Hz frequency, the strobe effect disappeared, as seen in Figure 3-8.

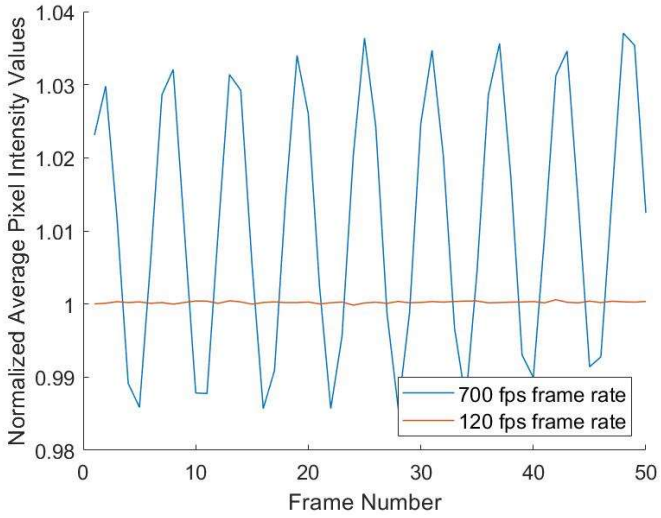

Figure 3-8. Normalized pixel intensity plotted to show the strobe effect of AC lighting as well as the solution. The blue line represents footage taken at 700 fps, illustrating the strobe effect, while the orange line represents footage taken at 120 fps, with negligible flickering [6].

Although the strobe effect was resolved by setting the frame rate to 120 fps, a notable consequence of this was a limitation on the time resolution of any data collected. Typical highspeed frame rates with Phantom cameras are 1 to 2 orders of magnitude higher than this. If available, a better alternative would have been DC powered backlights that produce zero strobe effects regardless of frame rate.

3.1.5 Optical Probe

As previously discussed, an optical probe consists of a light source and photodetector. In this case, the photodetector used was a power metered photodiode and the light source was a red dot laser diode. The power metered setup from Thorlabs can be seen in Figure 3-9 below.

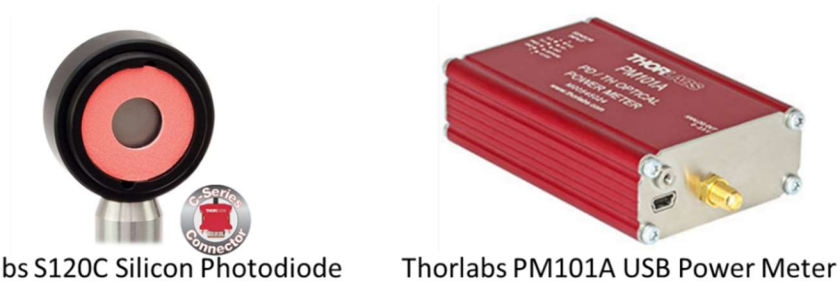

Figure 3-9. Thorlabs power metered photodiode setup.

A silicon photodiode was chosen for this setup because it offered sufficient accuracy, linearity, and responsiveness for this application at an affordable price. This Thorlabs S120C Silicon Photodiode had a very large active area relative to most photodiodes, making alignment much easier. Table 3-2 below lists the key characteristics for this setup.

Table 3-2. Thorlabs power metered photodiode characteristics.

Characteristic	Value
Accuracy (at 440-980 nm)	±3%
Linearity (at 440-980 nm)	±0.5%
Active Area	75 mm^2
Response Time	< 1 µs
Operation Mode	Zero Bias
Measured Output	Analog Voltage (0-2.5 V)
Power Range	50nW – 50mW

There are two operating modes for a photodiode: reverse-bias or zero-bias. Both modes have their strengths and weaknesses that are specific to the application. In reverse-bias mode, also known as photoconductive mode, a negative voltage difference is applied across the cathode and anode of the detector, and changes in the voltage difference are measured. The Thorlabs power metered setup in this study utilizes the photodiode in zero-bias mode, where no voltage potential is applied. Also known as

photovoltaic mode, a photodiode in this configuration produces a current that depends on the optical power and wavelength of the incident light. The power meter takes the current generated by the photodiode and feeds it into a transimpedance amplifier that is, effectively, a current-to-voltage converter [22]. Ultimately, the PM101A power meter outputs an analog voltage value that can be scaled based on a user determined constant V/W factor in Thorlabs' power meter software. This last feature was particularly useful in tuning the output voltage scale to best fit the incident power of the light source. Also, many applications with photodiodes pose a risk of oversaturation, especially in reverse-bias mode. This means that the sensor can be destroyed if the active area is accidentally exposed to an excess of light intensity. The zero-bias power metered setup was chosen due to the wide range of incident beam power the photodiode is designed to handle.

The light source used in this experiment was an inexpensive red dot laser, made by HiLetgo. The laser diode was powered with 5 VDC and had an adjustable lens cap for focusing the beam. A summary of the key characteristics of this diode can be seen below:

Table 3-3. Laser diode light source characteristics.

Characteristic	Value
Wavelength	650 nm
Measured Intensity	3.5 mW
Focused Beam Diameter	≈ 1mm
Operation Mode	Continuous

The spot size of the laser beam was roughly measured to be about 1mm in diameter when focused on a target 10" away (the set distance between the laser and the photodiode within the vessel). The spot roughly doubled in size when measured on targets 15" and 5" away, indicating that the beam was not well collimated across its path. To achieve a relatively constant beam diameter across the length of the enclosure, an additional precision collimating lens would have been required. Even without a well collimated beam,

this laser diode was adequate for use in this project. To allow for easier calibration and tuning of the probe, mounting hardware was 3D printed for the photodiode and laser module that enabled the devices to snap into a 1” pegboard.

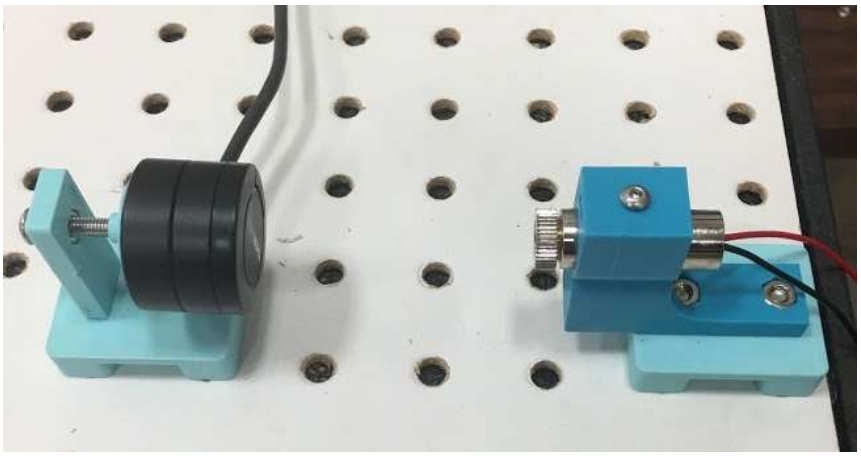

Figure 3-10. FDM printed device holders designed to snap into 1" pegboard for tuning and calibration.

To integrate these devices holders into the actual test apparatus, custom FDM printed mounts were designed to fasten into the diametrically positioned holes in the acrylic tube. These mounts included a track that the device holders could slide into, with a set screw to hold the devices in place.

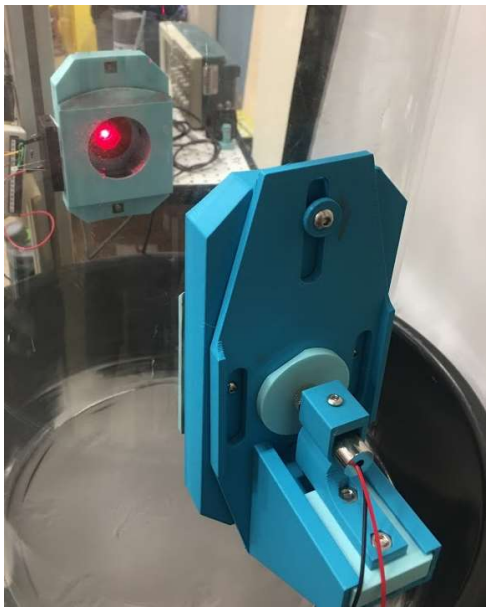

Figure 3-11. Optical probe mounting solution in the test apparatus using custom 3D printed hardware.

These mounts provided for translational adjustability to account for the low positional tolerances achieved for the drilled holes in the cylinder. This adjustability ensured that the entirety of the laser beam struck the sensor's active area when mounted to the vessel. Additionally, these mounts effectively sealed the holes in the cylinder such that a negligible amount of dust could escape.

3.1.6 DAQ and Control (LabVIEW)

A custom LabVIEW program was executed with a NI 6008 USB DAQ. This controlled the probe data acquisition and activation of both the dust dispersion system (via the motor driver) and a timing LED for synchronizing the camera footage and probe data. For a complete wiring schematic, reference appendix A.4.

According to technical support from Phantom, the ideal way to synchronize highspeed footage to data collection from a DAQ (such as the NI 6008) is to have the camera trigger serve as the trigger for the DAQ program to commence. Unfortunately, the camera model was too old to interface with the DAQ in such a manner, so another timing mechanism had to be devised. At the relatively low frame rate of 120 fps, it was feasible to run the footage prior to data collection and blink an LED when the LabVIEW program began collecting data. The blinking of that LED, which was in frame for the camera, was then used later to manually trim the footage accordingly. The location of this LED is shown on the next page in Figure 3-12. Although this synchronization method likely resulted in some timing error, the low frame rate allowed for this error to be considered negligible.

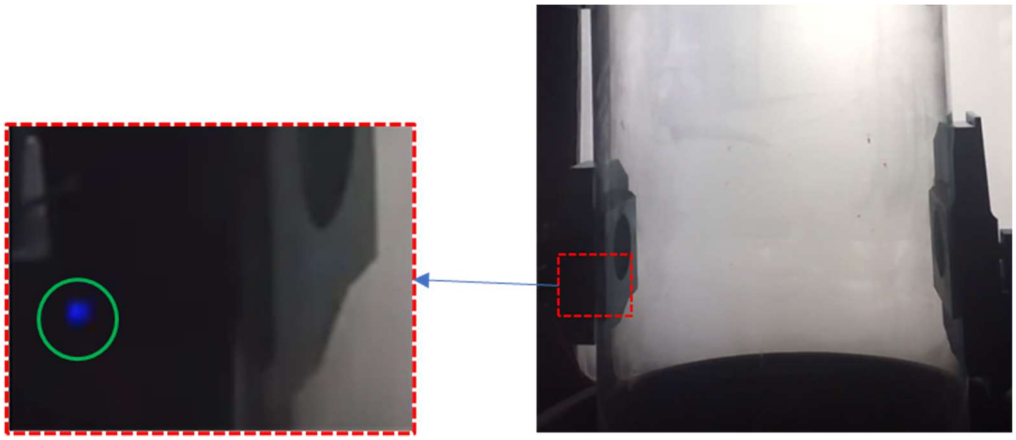

Figure 3-12. Placement of timing LED in the camera frame. This LED was set to blink once the LabVIEW program began collecting data from the probe.

To make post processing of data easier, the LabVIEW program collected and logged data at 120 Hz to match the frame rate of the camera footage. Specifically, the custom stacked sequence LabVIEW program included the following steps:

1) Take initial probe reading before dust had fallen (for normalization)
2) Turn on LED for approximately 10 frames (time duration = 10 frames / 120 fps)
3) Turn off LED
4) Send pulse to motor controller to initiate dust dispersion
5) Log data from probe for 6 seconds
6) Turn on LED again for 10 frames (to signify the end of the data collection)
7) Turn off LED and save probe data as CSV file

3.2 Data Post Processing

All post processing of the data for both the camera footage and the data was completed in a custom MATLAB script. The image analysis portion of this experiment was adapted from research by Lampshire [6].

3.2.1 Application of Theory

Section 2.5 presented the ways an experimental setup could apply BBL law to calculate a mass concentration value over time for a dust cloud. First, it was determined whether the sensor was located sufficiently removed from the particles such that the extinction paradox could occur. Applying Eqn. (8) to the probe with particles of about 28μm in diameter, a 650 nm light source, and the sensor active area of 75 mm^2 (9.77 mm diameter), the "sufficiently removed" distance required was found to be approximately 3 meters. Considering that the furthest distance possible between the sensor and any of the particles was about 0.26 meters, the application of the extinction paradox was not possible for the probe. For the camera, assuming an average intensity of about 570 nm from the full spectrum fluorescent backlight [23], the distance would be roughly 1.5 meters – again, too far for the extinction paradox to occur; however, this could be explored in future applications.

As discussed in section 2.5.2, two methods allow for the characterization of the extinction efficiency when the sensor is in proximity to the powder cloud:

1) Physically blocking out all forward scattered light ($\overline{Q} = 2$)
2) Rigorous experimental calibration ($1 \leq \overline{Q} \leq 2$)

In this experiment, the time and resources were not available to pursue either of these options in a rigorous enough manner to confidently characterize the extinction efficiency. Additionally, potential agglomeration of the particles within the cloud would need to be accounted for to characterize the Sauter mean diameter. Consequently, it would be theoretically misguided to suggest that a mass concentration value could be determined from either the probe or camera data collected in this experiment.

The next most physically informing metric from BBL Law relating to the amount of dust presence was the average extinction coefficient, $\overline{\beta}$, with units of cm^{-1}. Quantifying dust presence with the extinction coefficient is commonly practiced in the realm of fire protection engineering during smoke obscuration studies, where the term *smoke density* is used synonymously with the extinction coefficient [24].

Rearranging and substituting Eqn. (2) and Eqn. (5), the average extinction coefficient can be solved for.

$$\bar{\beta} = \frac{-\ln(T)}{\ell} \qquad \text{Eqn. (11)}$$

Theoretically, the path length is defined by the distance light travels through the attenuating medium. However, as the shape and size of the powder cloud was not consistent over time, this had to be slightly modified to describe the distance that the attenuating medium *could* occupy [7]. The implications of this will be further discussed in section 5.1.2.

3.2.2 Finding Extinction Coefficients over Time from Raw Data

This section details the custom MATLAB script that was used to ultimately back out the average extinction coefficient over time for both the probe and camera data using Eqn. (11). A flowchart of how this script functioned is depicted below in Figure 3-13.

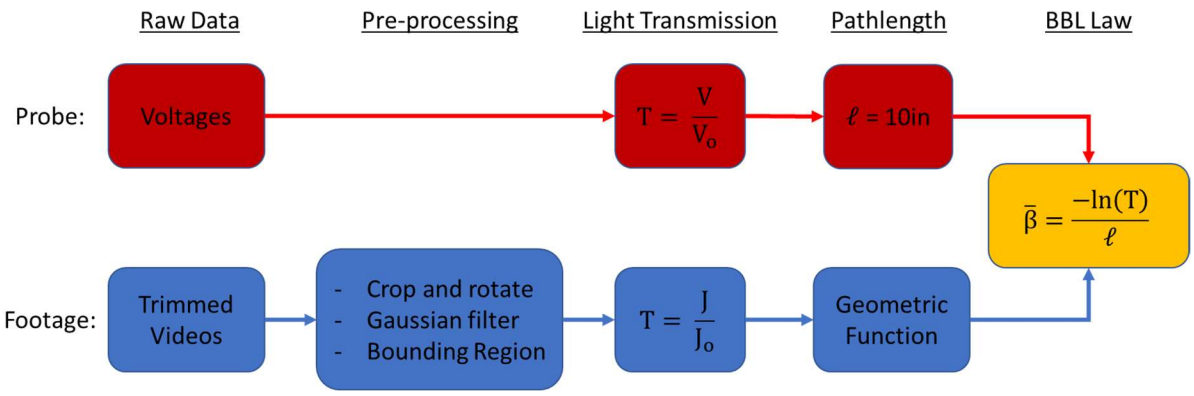

Figure 3-13. Flow chart of how the post-processing MATLAB code applied BBL Law to the probe and footage data.

A key assumption that was made and later corroborated (discussed in section 3.3), was that the photoelectric sensor in both the camera and the probe produced a linear and constant response to incident light over the range of wavelengths and intensities seen in this experiment. Different methods had to be

employed in the post-processing steps to get the probe and camera data. These steps are detailed in the following subsections and cover how the raw data from both the probe and footage were processed into the same form: a *n by m* matrix of extinction coefficients over time, with *n* trials and *m* data samples in each trial. Ultimately, with 12 successful trials and 600 data samples/frames from each trial, a 12 x 600 matrix of average beta values was created for both the probe and footage.

3.2.2.1 Application of BBL Law to Probe

Applying BBL Law to the probe setup was relatively straightforward. The measured output from the Thorlabs power metered silicon photodiode was an analog voltage reading, and was applied to Eqn. (11) via the following relationship:

$$T = \frac{V}{V_0} = \frac{I}{I_0} \qquad \text{Eqn. (12)}$$

The initial voltage reading was taken before each trial began with no dust present in the vessel. The LabVIEW program output a CSV file of all the raw voltage readings collected during the trial, which were extracted in the MATLAB program. The light transmission over time was calculated, and then this was fed into Eqn. (11). The path length used for the probe was fixed at the dimeter of the cylindrical vessel, at 10 inches.

3.2.2.2 Application of BBL Law to Footage

The post-processing of the footage data utilized previous research that created image processing methods to analyze dust cloud data. Relevant pieces of the code from Lampshire's research were adapted to be used in this experiment [6].

The method in which a camera captures grayscale footage is similar to the functionality of the probe. The photoelectric sensor on the Phantom v310 is a Complementary Metal Oxide Semiconductor, or CMOS, and is a grid of tiny photodiodes. The measured light intensity from each photodiode dictates the darkness of a corresponding pixel in the resultant image [25].

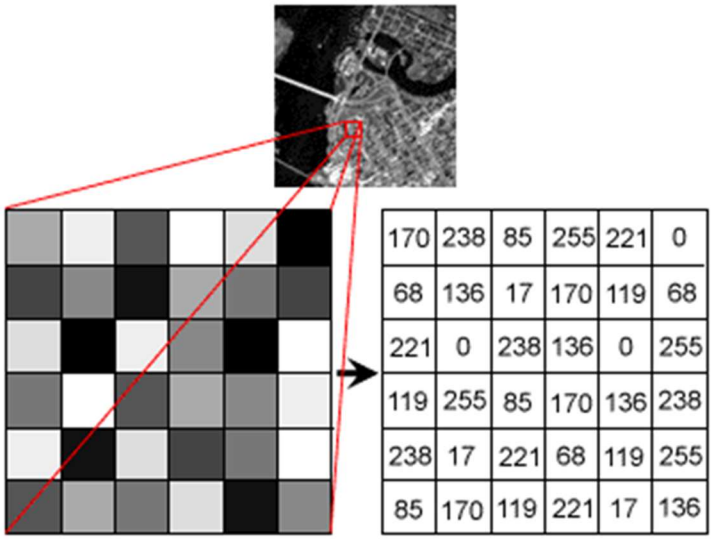

Figure 3-14. Illustration of how grayscale images are formed via a cluster of pixel intensity values ranging from 0 (black) to 255 (white) [6].

As shown above in Figure 3-14, a grayscale image is represented in MATLAB as an array, with each value signifying the light intensity of the pixel and corresponding location in the image. The values of grayscale light intensity are stored as 8-bit data values and range from 0 (a black pixel) to 255 (a white pixel) [26].

The MATLAB program used in this thesis analyzed the footage by looping through each frame to determine the light transmission as it changed over time. In order to align the probe and footage datasets, the footage was trimmed based on the timing LED discussed in section 3.1.6. Additionally, all frames were pre-processed with an applied crop, rotation adjustment, and Gaussian filter [26].

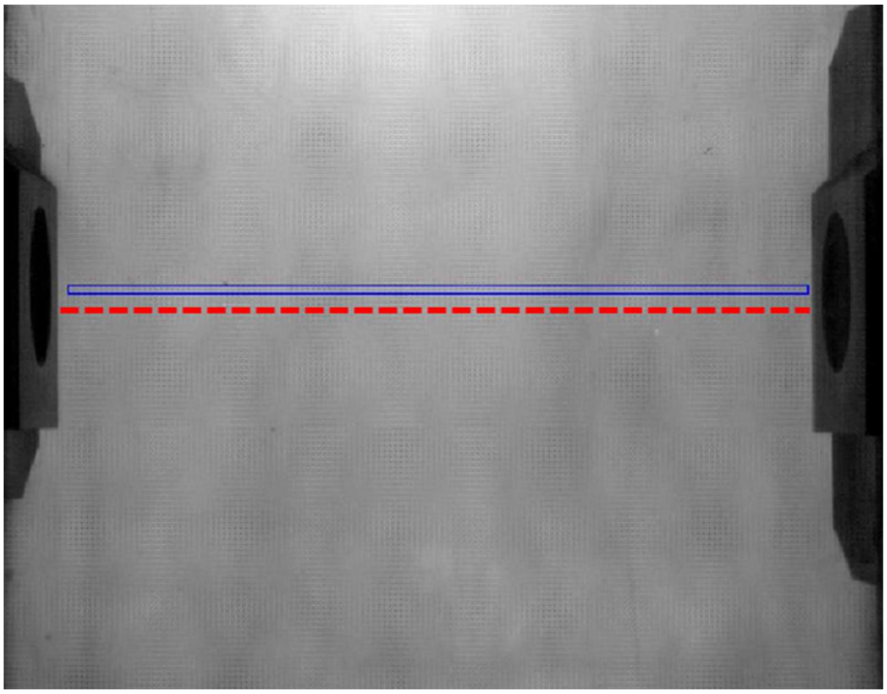

Figure 3-15. Frame from footage analysis showing the radial trace (in blue) and laser beam (overlaid with a red dashed line).

To prevent the visible 650 nm laser skewing pixel intensity data in the footage, the isolated region that represented the radial trace was placed slightly above the beam. This slight vertical offset, illustrated above in Figure 3-15, was calculated to produce a negligible timing error between the probe and footage data, discussed in further detail in appendix A.10.

Only the pixels within the isolated region were analyzed. The pixel intensities inside the isolated region were found for each frame. This transmission value for each pixel was calculated using the following linear relationship:

$$T = \frac{J}{J_0} = \frac{I}{I_0} \qquad \text{Eqn. (13)}$$

A difficultly when applying BBL law to the footage was that the pathlength was not constant across the frame due to the cylindrical cross section of the vessel. The varying pathlength, illustrated in Figure

3-16, was accounted for by developing a geometric mask that was applied to each frame, visualized in Figure 3-17 below.

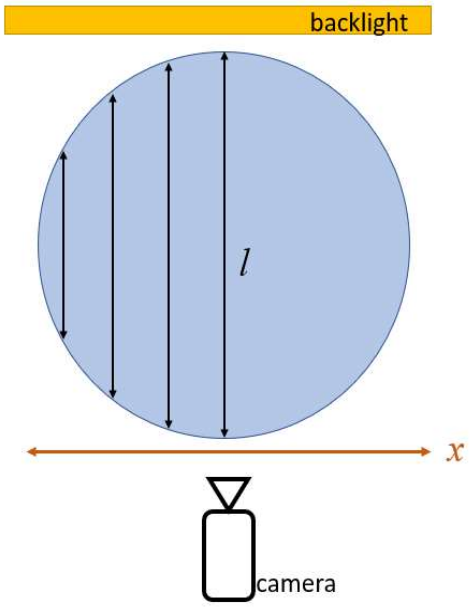

Figure 3-16. Diagram displaying the varying pathlength across the cylindrical enclosure [6].

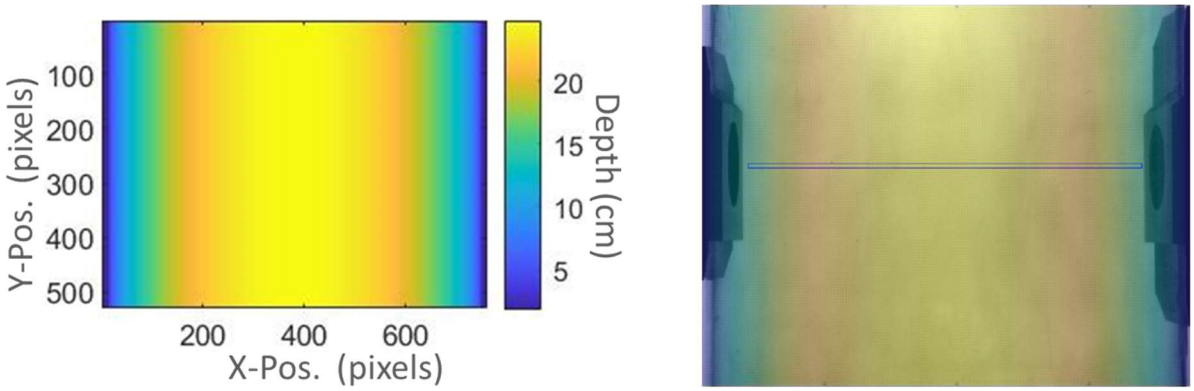

Figure 3-17. Visualization of the geometric mask used to match each pixel with its corresponding pathlength.

Each pixel's intensity and corresponding pathlength were applied to Eqn. (11) to produce an extinction coefficient value. The average of these values was taken to find the mean extinction coefficient

within the isolated region. This was repeated for each frame, determining the mean extinction coefficient over time for that trial.

3.2.3 Time Normalization of Trials

At this point in the post-processing, a 12 by 600 array of $\bar{\beta}$ over time had been created for both the footage and the probe data. Each of the 12 trials were plotted on the same graph, and a timing discrepancy was discovered regarding when the peak dust presence occurred for each trial. This error was attributed to inconsistencies with the powder cloud and determined to be within acceptable experimental error. The $\bar{\beta}$ matrix for both the footage and probe were ran through a custom MATLAB script to locate the onset of cloud detection within each trial via a gradient threshold. This start point was then used to shift the data within each trial, aligning all 12 trials with a set padding of time at the beginning.

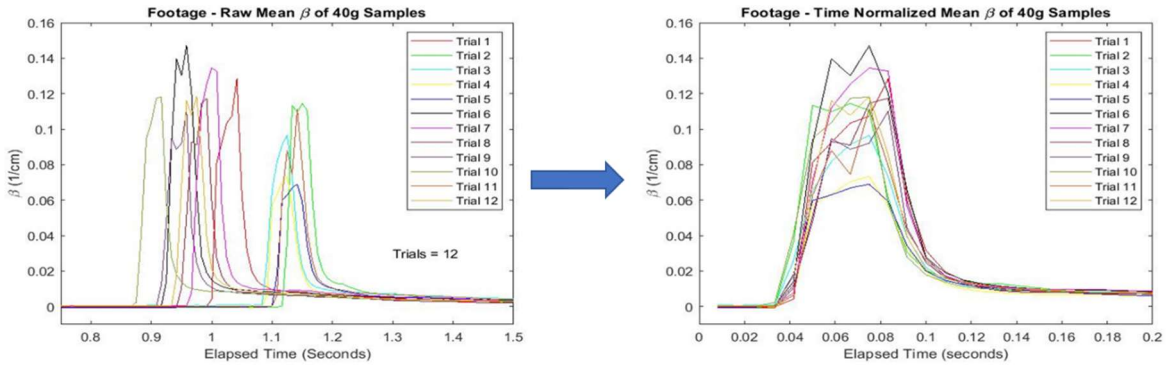

Figure 3-18. The data collected for both the footage and probe possessed timing discrepancies between trials. This was corrected by normalizing all trials to align at the onset of detected dust presence.

The result of this time shift script, plotted above in Figure 3-18, was a time-normalized $\bar{\beta}$ matrix for both the probe and footage, with all trials aligned by the onset of dust presence.

3.2.4 Statistical Analysis

Once each trial was aligned, statistical analysis was performed to back out a mean $\bar{\beta}$ over time for all 12 trials. This was done via a MATLAB script that looped through each column of the 12 x 600 time-

normalized $\bar{\beta}$ matrices, finding the mean, max, and min values of the column. Additionally, the upper and lower bounds of a 95% confidence interval were found for the data set in the column, using a normal T-distribution (due to the statistically small sample size) [27].

3.3 Calibration

The calibration of both devices was imperative to validate the model assumption that both photoelectric sensors have a constant linear response.

3.3.1 Probe Calibration

The goals of the probe calibration in this study were to verify the linear response of the silicon photodiode, as well as to determine how much of a signal the sensor was outputting from solely the camera backlight (ambient lighting). The linearity of the photodiode's response was determined using various combinations of neutral density (ND) filters, each with a specified optical density. This process of adding different combinations of ND filters can be seen in Figure 3-19. The transmission values were found at each ND combination using Eqn. (12) where V_o was the measured voltage when the laser beam hit the photodiode without any ND filters on.

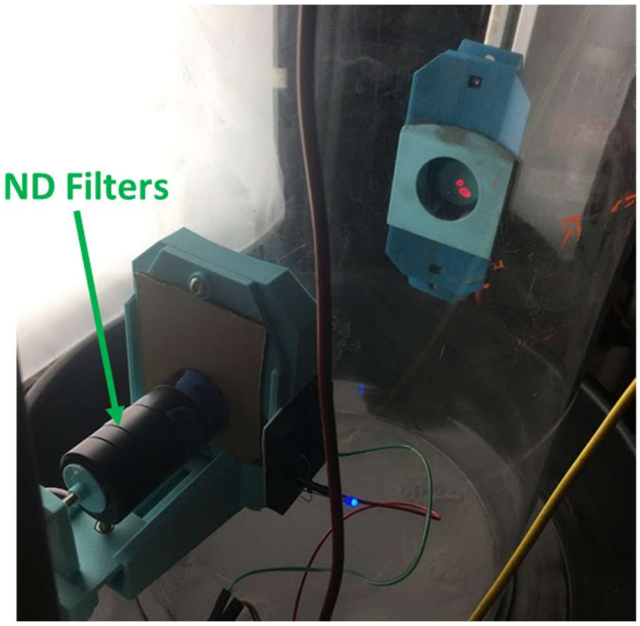

Figure 3-19. Probe calibration setup using various arrangements of neutral density (ND) filters to determine the linearity of the sensor.

This data was collected in a custom probe calibration LabVIEW program, shown in appendix A.7. The data was exported as a CSV file and plotted in MATLAB.

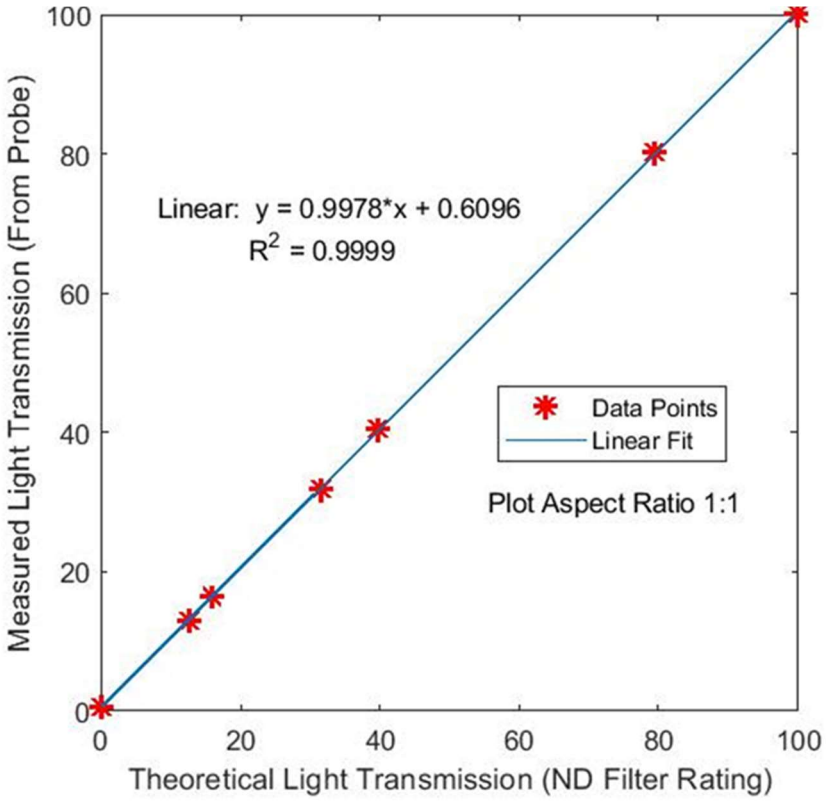

Figure 3-20. Probe calibration data plotted with a linear fit.

As shown in the linear fit data from Figure 3-20, the probe had an almost perfect positive linear fit with a 1:1 ratio between the measured and expected transmission values [27]. With the laser turned off, ambient light intensity was measured and found to be negligible.

3.3.2 Footage Calibration

Establishing a linear relationship between the incident light intensity and camera sensor response was not possible in this experiment, as no ND filters were available for this camera. The photoelectric sensor on the Phantom v310 camera was a Complementary Metal Oxide Semiconductor, or CMOS. These sensors are known to generally possess a maximum nonlinearity of about 2% [28]. This inherent nonlinearity error was determined to be acceptable given the scope of this study, and the CMOS in the Phantom camera was assumed to have a linear response to incident light intensity. Despite having to make that assumption, a calibration process was devised to check the following:

1) Ensure a constant response over time (no auto-adjustments occurring)
2) Find the blocked out light transmission value (influence of ambient light)

To investigate this, a strip of cardboard was spray painted flat gray to simulate what the vessel would look like if filled with a dense powder cloud, as shown below in Figure 3-21.

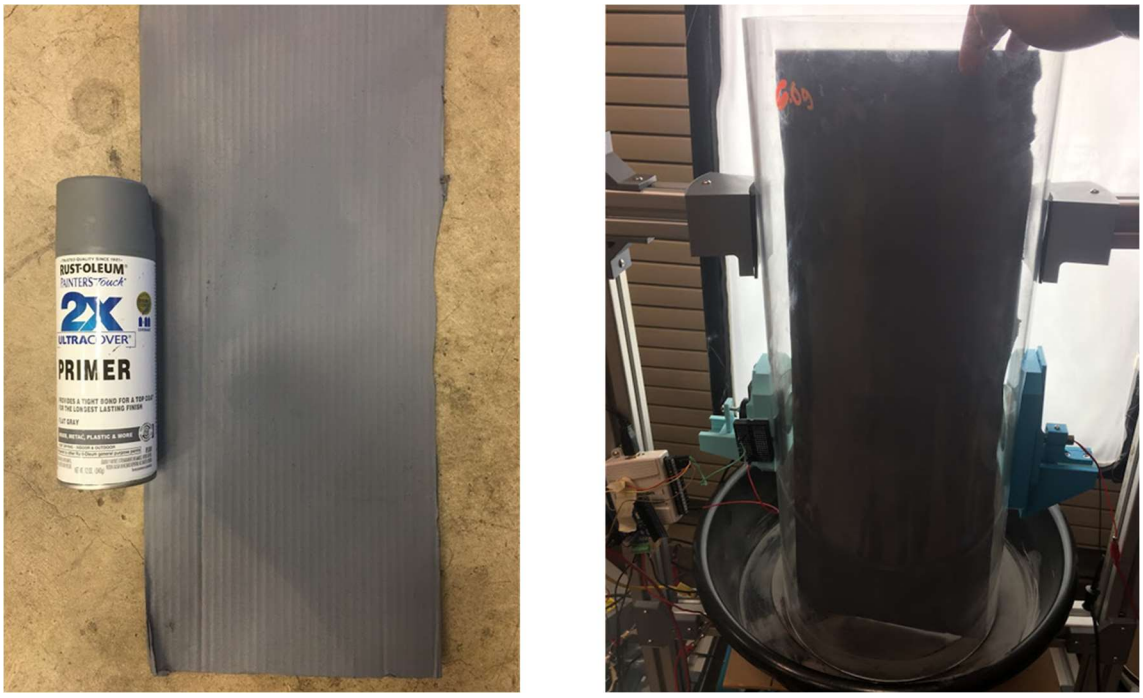

Figure 3-21. Spray painted cardboard strip used in footage calibration process.

This cardboard strip was lowered into the vessel while the camera was filming. In a video editing software, three frames were captured from the footage: one without the strip, one with the strip lowered halfway, and one with the strip completely blocking out the light from coming through the vessel. These three frames can be seen on the next page in Figure 3-22. Using that same video editor, the three frames were converted back into a video so that they could easily be processed through the same MATLAB script described in section 3.2.2.2.

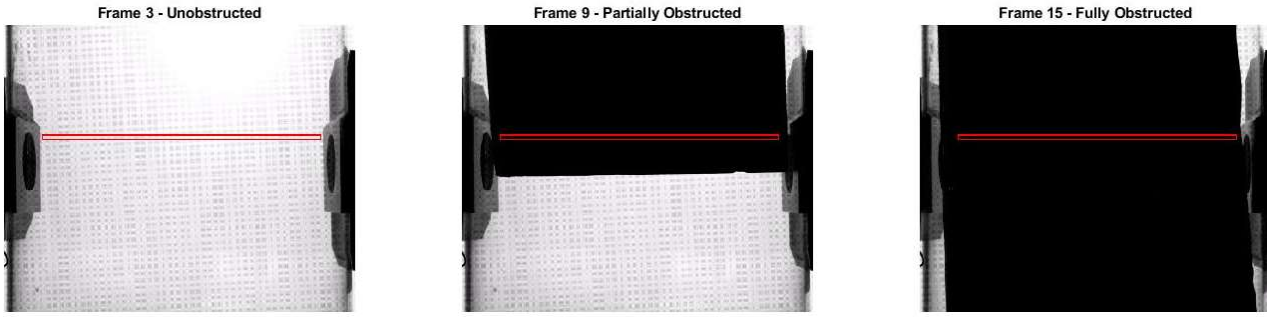

Figure 3-22. The three still frames chosen for the footage calibration process.

The unobstructed frame served as the reference, whereas the partially and fully obstructed frames were used to reveal any auto-correction occurring in the camera. In the latter two frames, the radial trace was fully obstructed by the cardboard strip – if the region was truly isolated from the rest of the frame, both frames would yield the same average pixel intensity. Essentially, this checks to ensure that no auto-corrections occur with the camera setup, something that is particularly important with digital cameras (reference appendix A.1).

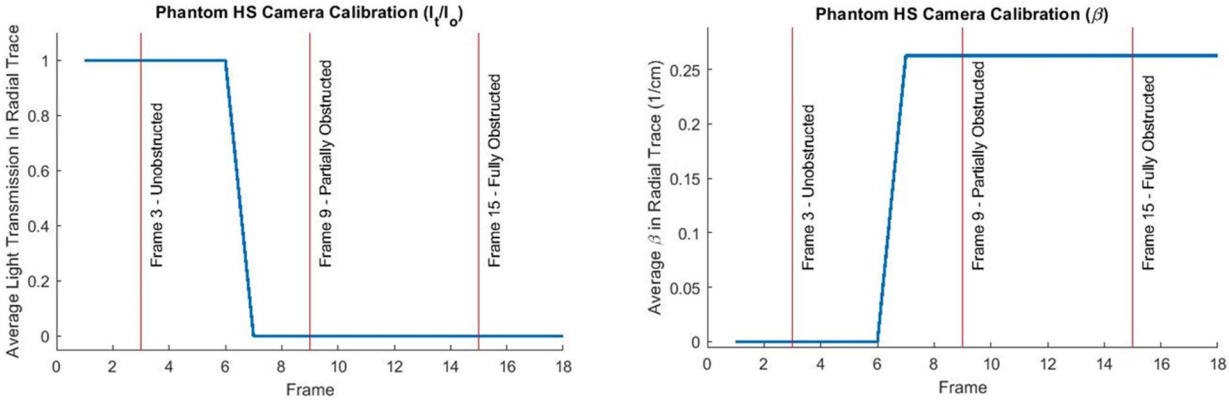

Figure 3-23. Results from footage calibration, validating that the CMOS sensor on the Phantom v310 has a constant response. Additionally, negligible light transmission was measured when the isolated region was fully obstructed.

As shown in the plots from Figure 3-23 above, no auto-corrections occurred with the Phantom v310 camera. Outside of confirming that no auto-corrections were occurring, the other feature this calibration process confirmed was a negligible effect of ambient light on the measured transmission value. When the

cardboard fully obstructed the isolated region, those pixels displayed a negligible light transmission despite the stray light surrounding the region.

4 Results and Discussion

At the end of the experimentation process, 12 trials had been collected that contained viable footage. This raw data was post-processed and analyzed using MATLAB, as detailed in section 3.2. After applying the statistical processing method explained in section 3.2.4, the corresponding probe data from all 12 successful trials can be seen below in Figure 4-1.

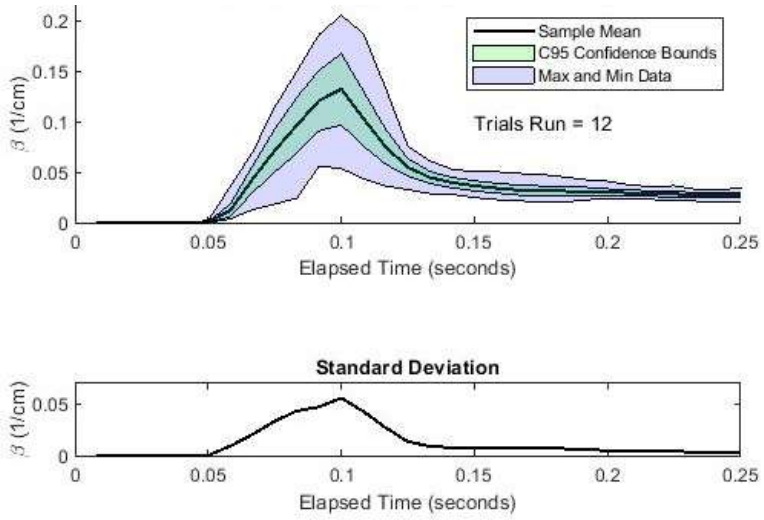

Figure 4-1. Probe mean extinction coefficient, 95% confidence interval (C95), data bounds, and standard deviation over time for the 12 viable trials. Data was taken at 120 Hz to match the frames per second of the highspeed camera.

For the remainder of this thesis, only the confidence bounds and mean curve will be shown on any figures – the max and min data will be removed to declutter the plots. The large spread in the data could be largely explained by the nonuniformity and variability of the powder cloud.

Figure 4-2. Snapshot of the cloud falling through the vessel, displaying the tendency of the powder to fall in plumes. This demonstrates the lack of uniformity within the powder cloud.

As shown above in Figure 4-2, the falling powder tended to clump and fall in plumes, leaving voids in the cloud that fluctuated both temporally and spatially between trials. The powder's tendency to clump was attributed to the dust dispersion method, specifically the ridges inside the deflector shield. The bowl that was used for the shield was chosen largely out of convenience, and the internal ridges were anticipated to help mix the cloud. However, through observing highspeed footage of the dust dispersion process, it appeared that powder may have clung to these ridges and accumulated before rebounding down into the vessel. This could have caused the plumes to form and, inadvertently, increased the nonuniformity of the cloud. Consequently, despite there being a consistent mass of powder dropped in each trial, the actual amount of powder that passed through the probe's laser beam fluctuated significantly between trials, leading to a large spread in the data.

4.1 Comparing Footage and Probe Data

The image analysis method presented in this section utilized two different types of boundary regions – a center box and a radial trace. Although the resultant extinction coefficient measurements extracted from the regions are different, it is important to note that both regions were applied to the same raw footage.

4.1.1 Center Box Region

First, a center box region was selected to gain a better understanding of how uniform or axisymmetric the dust cloud was. This region is visualized in Figure 4-3 below both in 3D space and in the 2D representation within a frame (reference Figure 3-1 for a 3D rendering with the camera position included).

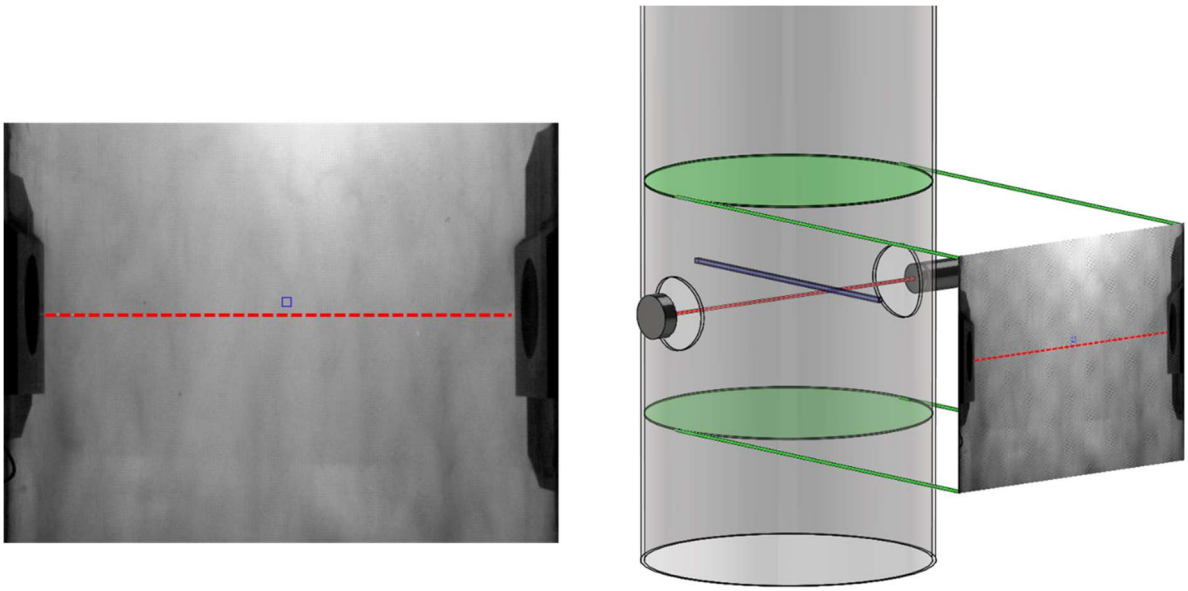

Figure 4-3. Center box region visualized in 2D and 3D space. The probe can be seen in red, while the bounding region of the center box is in blue.

Physically, this method was a direct comparison to the laser in that it turned the camera into more of a point source. However, because the camera's axis was perpendicular to the probe, only a uniform or axisymmetric cloud would enable these two data sets to align.

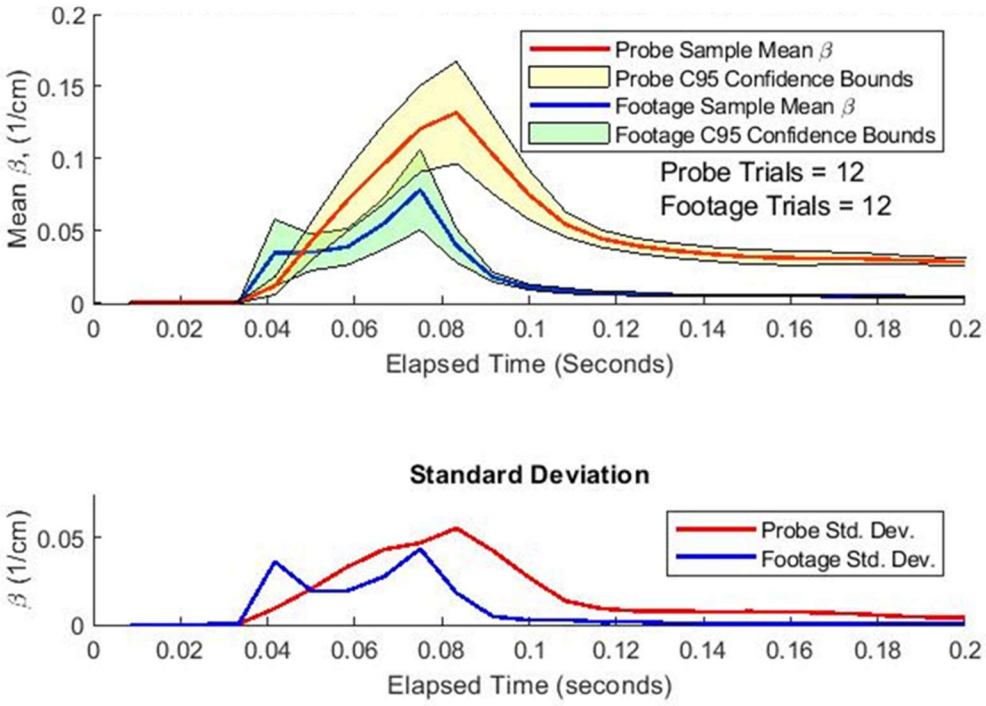

Figure 4-4. Overlaying the mean extinction coefficient over time with C95 bounds for both the probe and center box region.

As seen in the plots from Figure 4-4 above, the probe and center box data did not correspond well, highlighting a lack of uniformity and repeatability of the dust cloud between trials. The underlying reason for this, as discussed at the beginning of this section, was the nonuniformity and variability of the powder cloud likely caused by the design of the dust dispersion system. In any given trial with a nonuniform cloud, it was highly unlikely that a similar amount of dust would be observed by two point source measurements on axes perpendicular to one another. Furthermore, data from the center box region showed an unexpected trend of the dust cloud in the center of the vessel, where two peaks of average intensity occurred across the trials. From observing the footage, it was determined this was simply the result of some trials possessing little to no powder in the center box region, which skewed the mean of the data.

4.1.2 Radial Trace Region

The original objective given by LLNL for the footage analysis was to compare a radial trace following the same path, in frame, as the laser. There are several implications with this method that limit

the physical robustness of relating these two datasets. The fact that the probe and camera were aligned on axes perpendicular to one another and that the probe was, effectively, a point source measurement while the camera was condensing a 3D space into a 2D plane, limited the physical equivalency of the two measurements.

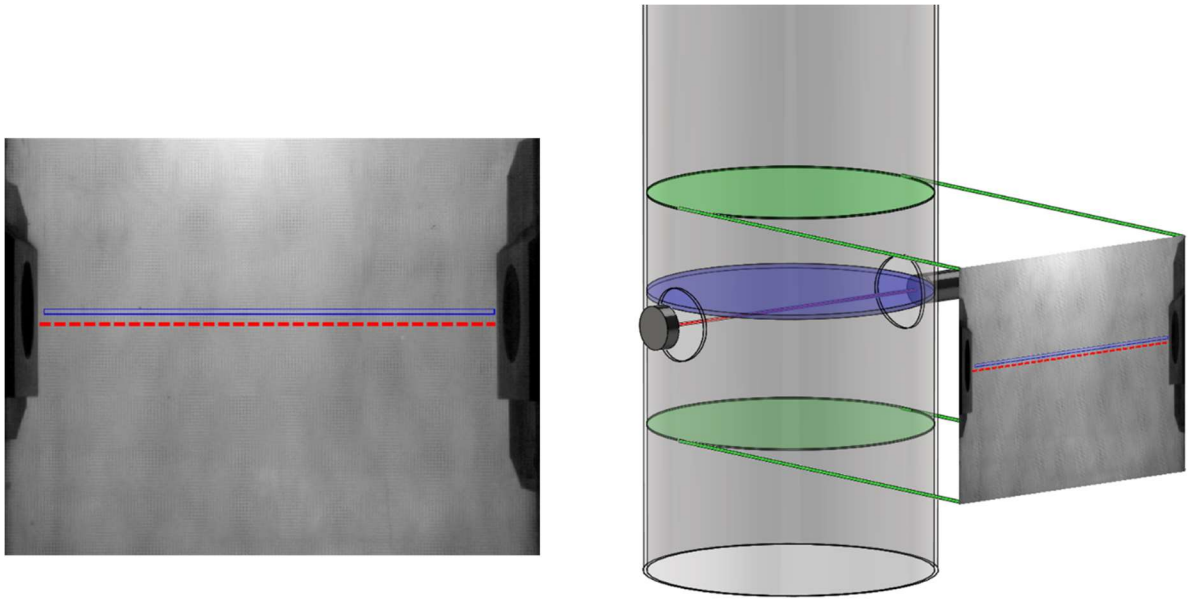

Figure 4-5. Radial trace region visualized in 2D and 3D space. The probe can be seen in red, while the bounding region of the radial trace is in blue.

The visualization of the radial trace in 2D and 3D space relative to the probe, shown above in Figure 4-5, highlights the differences between these two measurements. Spatially, the devices were measuring the dust cloud on axes perpendicular to one another. This would have been inconsequential if the powder cloud was approximately uniform or axisymmetric, but it was neither. Physically, the two devices were different in that the probe was a point source measurement, while the camera was a 2D plane. The means and confidence intervals from both methods can be seen overlayed in Figure 4-6 on the next page.

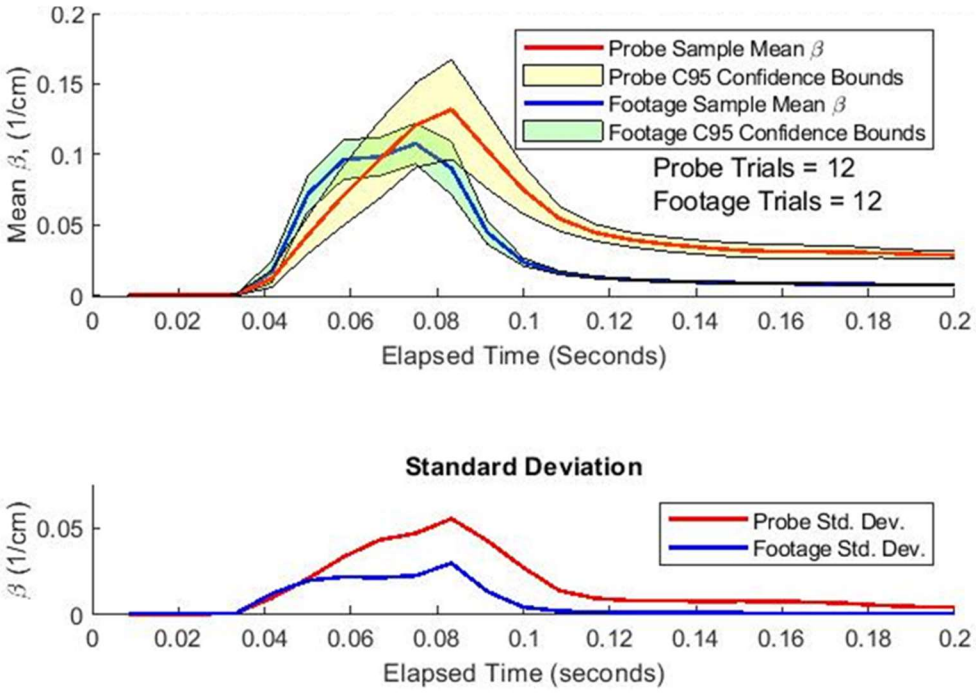

Figure 4-6. Overlaying the mean extinction coefficient over time with C95 bounds for both the probe and radial trace.

Despite the physical and spatial differences in what the two methods were measuring, Figure 4-6 shows that the general shape of the two datasets aligned well, especially relative to the center box region. There were two key aspects that explained the higher magnitude of both the standard deviation and average extinction coefficient for the probe. Due to the laser light source being collimated for the probe while the backlight for the camera was not, the photodiode on the probe was expected to measure less forward scattered light [7]. Referencing the theoretical bounds of the extinction efficiency stated in section 2.5.2, it was anticipated that the lack of scattered light seen by the probe detector would push the extinction coefficient closer to the upper bound of 2. Conversely, the lack of any collimation for the camera backlight would likely cause its CMOS sensor to measure more forward scattered light, leading to an average extinction coefficient being closer to the lower bound of 1 for the footage. This explained the following relationship that was observed in the data:

$$\overline{Q}_{Probe} > \overline{Q}_{Footage}$$

Applying this observed relationship to Eqn. (5), the following relationship was expected anytime that the footage and probe measured a similar amount of dust:

$$\overline{\beta}_{Probe} > \overline{\beta}_{Footage}$$

This expectation of the $\overline{\beta}_{Probe}$ being greater than $\overline{\beta}_{Footage}$ was confirmed in the data. Outside of the theoretical expectation for this relationship between the extinction coefficients, it was also further explained by how the probe averaged a smaller portion of the cloud than the radial trace. In this study, the cloud created was not uniform, with tungsten powder clumping together and falling in plumes. With this type of cloud, there was a greater number of voids left uncovered by the powder that could be averaged into the radial trace's larger area. This potentially served to lower the average extinction coefficient of the radial trace relative to the probe. Additionally, this difference in area made the probe substantially more sensitive to fluctuations in the cloud than the radial trace, leading to the expectation of the following relationship for the standard deviations of the two methods:

$$SD_{Probe} > SD_{Footage}$$

As expected, the experimental standard deviation of the probe was almost double that of the radial trace method.

4.2 Correlating Radial Trace and Probe Data

After determining that the average $\overline{\beta}_{Probe}$ was greater than the average $\overline{\beta}_{Footage}$, the next step was to determine whether a numerical correlation could be made between the two values. To extract values for this, the time duration of the cloud passing by the radial trace and probe had to first be established. This approximated duration can be seen in Figure 4-7.

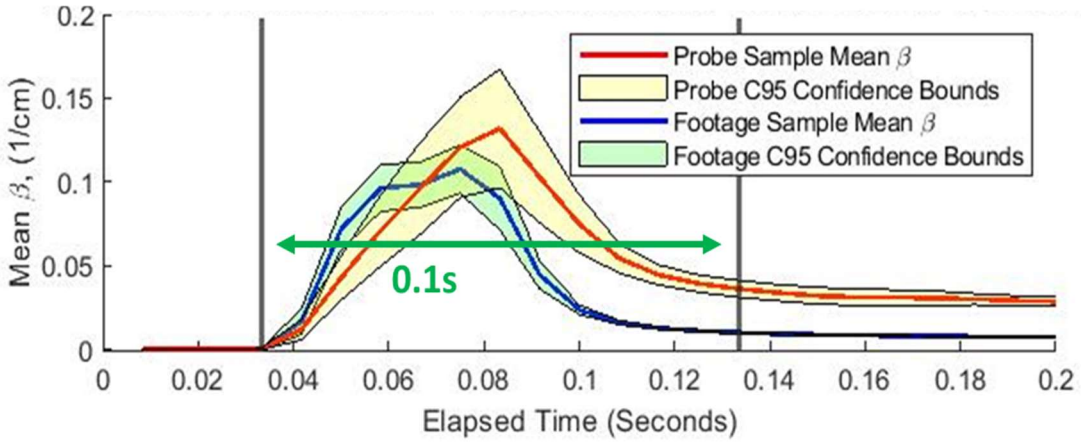

Figure 4-7. Approximate time duration of a dust cloud passing by both devices. This time was estimated, by visual inspection, to be about 0.1 seconds.

An average $\bar{\beta}$ (a single value) was found for both the probe and radial trace in each trial by taking the mean of all extinction coefficient data points from that single trial that occurred during the time duration of 0.1 seconds, as shown above in Figure 4-7. To determine if a numerical correlation existed between the two datasets, the average $\bar{\beta}_{Footage}$ was plotted against the average $\bar{\beta}_{Probe}$ for each of the 12 trials in an x-y scatterplot. Additionally, the max $\bar{\beta}$ was also found for each trial and plotted in the same manner.

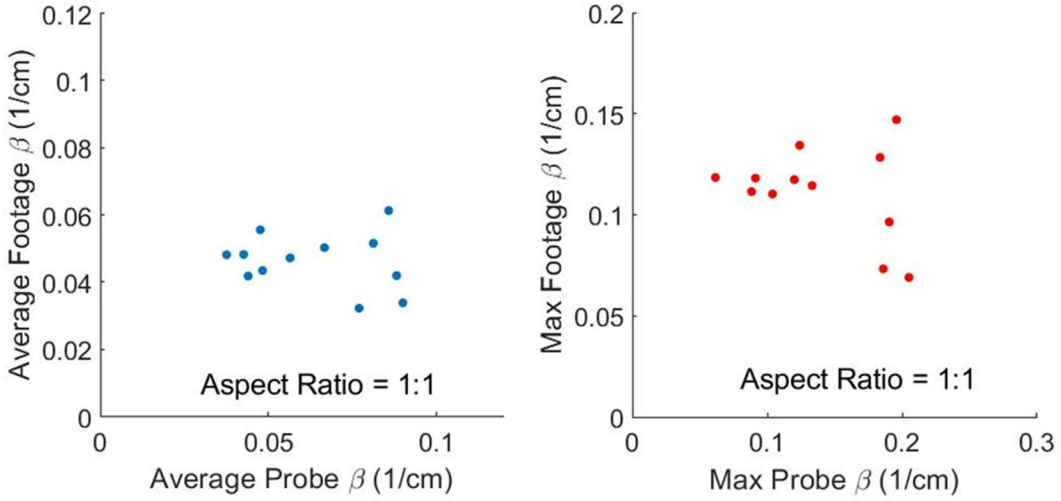

Figure 4-8. Scatter plots checking if any correlation exists between $\bar{\beta}$Probe and $\bar{\beta}$Footage in this setup. The 12 blue dots represent the average probe and radial trace values plotted against for each trial, while the red dots are for the max values plotted against each other.

As shown above in Figure 4-8, there was no discernable correlation between the probe and footage measurements that could be concluded from the data collected in this experiment.

4.3 Error Bounds for Measuring Concentration with Current Setup

As discussed in section 3.2.1, there was no way to confidently back out a mass concentration value from any of the data collected due to the limitations of the experimental setup. Specifically, there was no means to adequately characterize the agglomeration factor, α, and the average extinction efficiency, $\overline{Q}$. A study was done to see what error bounds could be expected for a mass concentration value if Eqn. (6) were to be applied to a trial of probe data without knowing $\overline{Q}$ and α. The results of this study are plotted below in Figure 4-9.

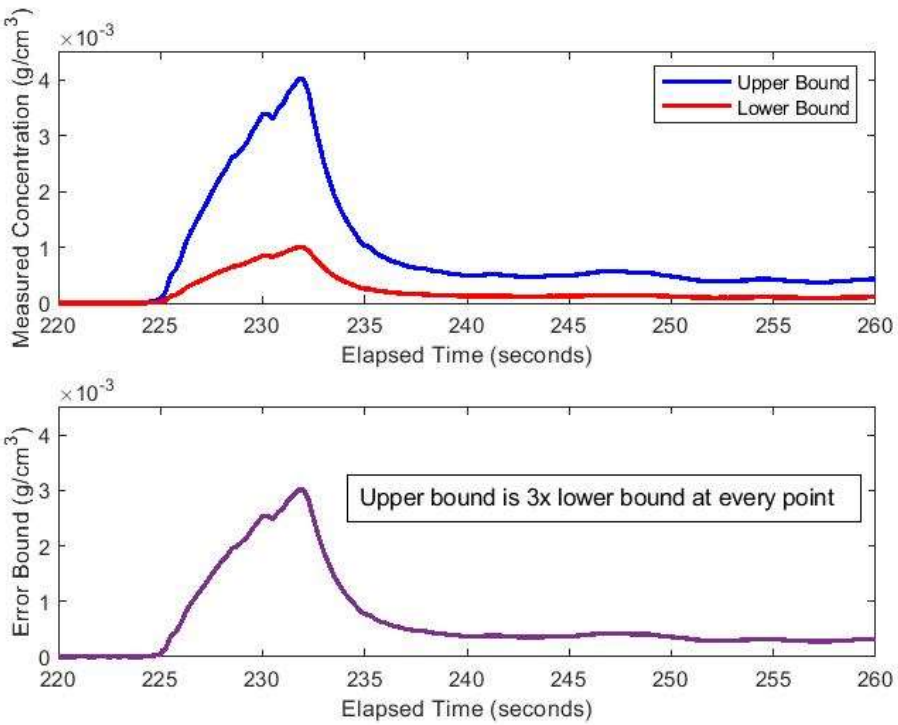

Figure 4-9. Plot showing the measured mass concentration in g/cm^3 for one of the probe trials. The upper bound uses $\overline{Q} = 1$ and $\alpha = 2$, while the lower bound uses $\overline{Q} = 2$ and $\alpha = 2$. The bottom subplot is the difference between the two bounds over time.

As discussed in section 2.5.2, the bounds for $\overline{Q}$ in this study were $1 \leq \overline{Q} \leq 2$. Not much data was available to inform an educated guess for the agglomeration factor bounds. The lowest possible value would be $\alpha = 1$, meaning that no agglomeration occurred. The most relevant information found was from a report documenting the agglomeration of nanoscale aluminum AM powder when dispersed in a cloud. This report found agglomeration factors of $\alpha = 4.6$ and $\alpha = 1.7$ for samples with average diameters of 35 nm and 100 nm, respectively. The paper highlighted a significant drop off for the agglomeration factor as particle size increased. If tungsten AM powder behaves in a similar manner, there is reason to expect that the agglomeration factor for microscale tungsten AM powder would be close to $\alpha = 1$ [18]. Despite this, the conservative upper bound used in the plot was $\alpha = 2$, referencing findings by PRL in the Three Probes study with some of their microscale dust samples [7].

5 Conclusions and Recommendations

One of the main accomplishments of this thesis was the development of a methodology that was able to quantitatively determine dust presence over time inside an enclosed area. With the modifications detailed in section 5.2, this method could be adapted to reliably calculate the mass concentration of a powder cloud inside a dust explosibility chamber.

Another key accomplishment was a summarization of the relevant theoretical assumptions and limitations of Bouguer-Beer-Lambert law, detailed in Table 2-1. That table also listed the necessary modifications to some theoretical assumptions to allow BBL law to be applied in this experiment, along with the corresponding precedent for each modification. In section 2.5, the bounding cases of the extinction efficiency were discussed with respect to the sensor's distance from the shadow region of the particles. A criterion, Eqn. (8), was extrapolated from published theory to determine if a sensor is sufficiently removed from the particles it is measuring such that it avoids detecting any forward scattered light from them [12]. When the sensor is not sufficiently removed, as was the case for these optical dust probes and camera, the bounds of the extinction efficiency were determined to be:

$$1 \leq \overline{Q} \leq 2$$

The lower bound extinction efficiency of $\overline{Q} = 1$ occurs when a sensor sees all scattered light from a particle, and only the light geometrically incident to the particle is blocked. The upper bound extinction efficiency of $\overline{Q} = 2$, the extinction paradox, occurs when all scattered light is blocked from reaching the particles [7]. When the sensor is in proximity to the cloud, the two options to characterize the extinction efficiency are to either physically block out the forward scattered light with precision optical devices, or to go through a rigorous calibration process. It was determined that ensuring the probe setup is adequately designed to block out forward scattered light is the optimum manner through which to characterize the extinction efficiency.

5.1 Challenges and Limitations

Perhaps the largest challenge faced when completing this work was that it was during a pandemic that upended most aspects of society. COVID-19 made everything, from receiving parts to generally staying sane and productive, very difficult. However, COVID-19 was not the only challenge faced over the year of working on this project, and the following subsections serve to document the more technical limitations of this thesis.

5.1.1 Technical Challenges

Some of the key technical challenges that occurred during this thesis were:

1) *Being limited to an AC camera backlight, and thus having a max sample rate of 120 Hz.*

   This, combined with a dust cloud of heavy tungsten powder that fell quite quickly, meant a lack of time resolution for the data collected.

2) *Not being able to test on LLNL's clear pressurized vessel.*

   Having to design and build a test apparatus at Cal Poly was a time-consuming endeavor that, ultimately, was unable to produce a uniform or repeatable dust cloud (discussed in 5.1.2). The data collected for this thesis would have been greatly improved if testing could have been conducted with pre-existing LLNL's transparent vessel.

3) *Using an outdated and slightly damaged highspeed camera.*

   The Cal Poly Mechanical Engineering Department was generous enough to loan a Phantom v310 camera to students for projects, which was instrumental in the completion of this thesis. However, the camera had some issues in that it was both an older model and damaged from being dropped by students over the years. Not being able to synchronize the highspeed camera with the NI USB 6008 DAQ was less of a challenge at the low framerate used; however, this would have streamlined the data collection process and would have been requisite had filming occurred at true highspeed framerates. The damage to the camera limited the amount of successful trials, as the camera would

frequently malfunction while filming. The randomness of the camera's ability to capture viable footage was ascribed with a mysterious anthropomorphistic personality and working with the camera quickly devolved into a superstitious affair.

5.1.2 Issue of Cloud Nonuniformity

All modifications made to the theoretical assumptions of BBL Law in section 2.4 were backed up with precedent. However, in the application of BBL Law to this setup, a concern regarding the degree of nonuniformity seen in the tungsten powder cloud remained unassuaged.

Uniformity of the powder cloud is a key assumption made when applying BBL law, specifically regarding the definition of pathlength. Theoretically, the pathlength describes the distance light travels through a perfectly homogeneous, dispersed, and uniform attenuating medium. There is precedent to modify that definition to fit the application of measuring a powder cloud that changes shape over time, redefining pathlength as the distance that the powder *will* or *could* take up when the cloud forms [7]. However, this dynamic model of pathlength has almost entirely been utilized in experiments involving lightweight dust samples, not heavy AM metal powders. For example, one of the primary references for this paper, the Three Probes study, tested on powders from the mining industry [7]. One of the powder samples from that study, coal dust, has a solid density between 15-20 times less than tungsten AM powder. This is an important distinction, as lightweight powders are able to suspend in the air when dispersed, while tungsten powder was observed to clump and fall rapidly to the bottom of the chamber. No precedent could be found to support applying BBL law in this circumstance where the powder tended to fall in plumes with randomly occurring voids in the cloud. However, determining the degree of nonuniformity that would prevent the application of BBL law would require further research and was beyond the scope of the thesis.

One potential solution to this problem could be to alter the purpose of the radial trace image analysis. Data from the radial trace can numerically determine where dust is located at any given point in

the vessel. This information could be used to produce a dynamic pathlength value over time for the probe that excludes voids. A very basic illustration of this concept can be seen below in Figure 5-1.

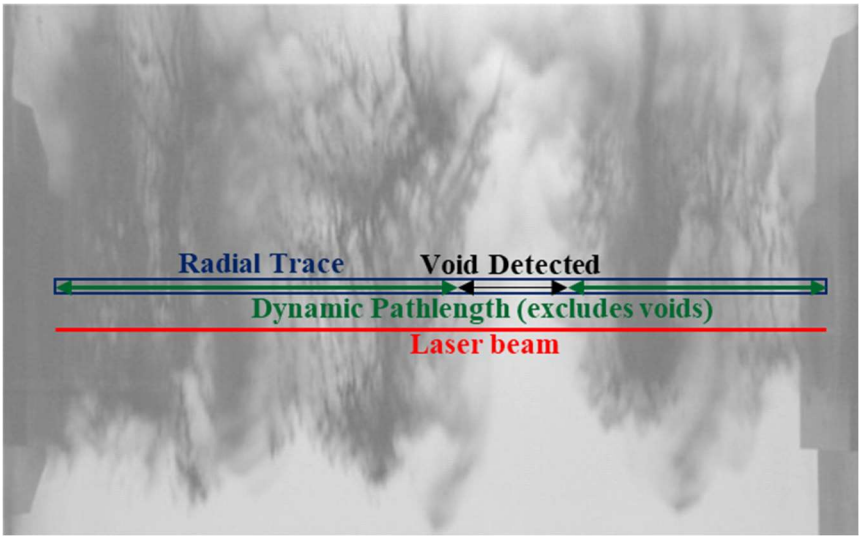

Figure 5-1. Basic illustration of a potential functionality for the radial trace method, where pixel intensity thresholding is used to detect voids in the powder cloud. This could determine a dynamic pathlength value for the probe in situations with nonuniform clouds.

This dynamic pathlength could then be applied to the probe in data post-processing, potentially allowing the probe to be applied to nonuniform clouds with a closer adherence to the theoretical assumptions of BBL Law.

5.2 Recommendations

5.2.1 Modifications to Experimental Setup

The path towards calculating a mass concentration value for the probe would first involve a lens and aperture setup to physically block the forward scattered light, as well as upgrading the light source to a more collimated laser. Narrowband optical filters would also be beneficial to block out undesired wavelengths, specifically impeding the majority of any scattered light produced by the camera backlight passing through the cloud [7]. With these adjustments, the average extinction efficiency could confidently be assumed to be $\overline{Q} = 2$. An understanding of the agglomeration factor for the powder in the cloud would also be required.

The highspeed camera setup was one of the weaker links in the overall experimental design. Some of the immediate recommendations would be to use a DC backlight and a newer camera model that is capable of interfacing with the DAQ, allowing true highspeed framerates. A monochromatic and collimated backlight system would likely be difficult to obtain; however, addressing either of these aspects for the camera light source would serve to remove doubt on the application of BBL law to the image analysis method. Additionally, the process for calibrating the highspeed camera was incomplete, as it lacked the ability to assess the linearity of the CMOS sensor. It is recommended to obtain Neutral Density filters that fit the highspeed camera lens and complete a similar process to the probe calibration from section 3.3.1. This would be in addition to the calibration process for the camera detailed in section 3.3.2 that checks for any auto-adjustments occurring in the footage.

The statistical analysis performed on the data in this thesis could be expanded upon. Particularly, some of the trials were likely to have possessed exceptionally nonuniform clouds, and it is recommended that future studies involve a method to identify outliers. One such method is an X-bar and R control chart that could be very useful to identify, assess, and potentially remove outlying trials, refining the data [27].

The dust dispersion method worked well considering the lack of immediately available resources. Switching to a pressurized dispersion method, such as the transparent vessel developed by LLNL, would be ideal. However, it is quite likely that changing out the deflector shield used with the dust dispersion method could produce a more uniform cloud – specifically, a bowl that does not have internal ridges could eliminate some of the observed streaking effects. As discussed in section 4.2, no correlation existed between the probe and radial trace footage in this study. Despite the physical differences in the radial trace and probe data, further research could establish a correlation with a highly uniform cloud. Instead of investigating this with heavy metal AM powders, it is recommended to develop an apparatus that uses smoke as the attenuating medium. Creating a uniform cloud would likely be far easier with the small and low-density solid particulate in smoke, which could suspend and evenly disperse inside a chamber. This is commonly done in fire protection engineering when verifying the accuracy of smoke detectors via a “smoke

box", which is used to fill a vessel with an evenly distributed set concentration of smoke [29]. Furthermore, creating an intentionally nonuniform cloud could be controlled much more readily with smoke, allowing for a study that determines the degree of nonuniformity that BBL law can apply to. Generally, creating a setup that allows smoke to be the attenuating medium would serve as a good baseline for calibrating the methodology so that it can verifiably apply BBL law. Once this is complete, heavy metal AM powders could be reintroduced with more confidence.

One of the big limitations of this study was that information from a 3D cloud of dust was trying to be measured by a single probe and a single camera. Augmenting the setup to allow for 3D measurements could greatly improve the ability to characterize features within the cloud. This could be done for either the camera or probe by simply using multiple devices or using a single device with a mirror or reflector setup. It would be straightforward, and highly recommended, to incorporate multiple probes at once to collect more data. Another means of gaining more information from a single probe could be to use reflectors within the vessel to bounce the light around the cloud before detection, allowing the pathlength to not be restricted to a straight line. For the camera, filming at an off-axis or tilted plane relative to the probe could also help produce a better understanding of the clouds uniformity than the view used in this experiment.

5.2.2 Integrating Probes Inside ANKO Vessel

When incorporating these probes into the ANKO vessel, fiber patch cables could be used to remove the photodiode and laser from the vessel. This was experimented with briefly in this thesis, but a precision mounting system would have been required for alignment. This was not available for this thesis, so proper testing was unable to be completed. However, it is expected that the flexibility and robustness of a fiber patch cable setup could be a great means to apply these probes to the harsh environment inside the ANKO vessel.

A common issue with dust particles of any form is the buildup of static charge. If accidental deflagration is a concern for the powder being used, static charge buildup can serve as a potential ignition

source. Static charge buildup also causes powder to clump together and stick to any ungrounded surfaces. The difficult part of this in any experimental setup involving highspeed footage is that standard clear materials, such as glass and plastic, do not possess a surface conductivity through which it can be electrically grounded. In the Three Probes study, PRL researchers had difficulty with powders sticking to the lens covers of their probes inside of the 20L vessel. Their solution was a complex setup that directed a localized jet of air over the lens shield to prevent dust from accumulating on it, shown below in Figure 5-2.

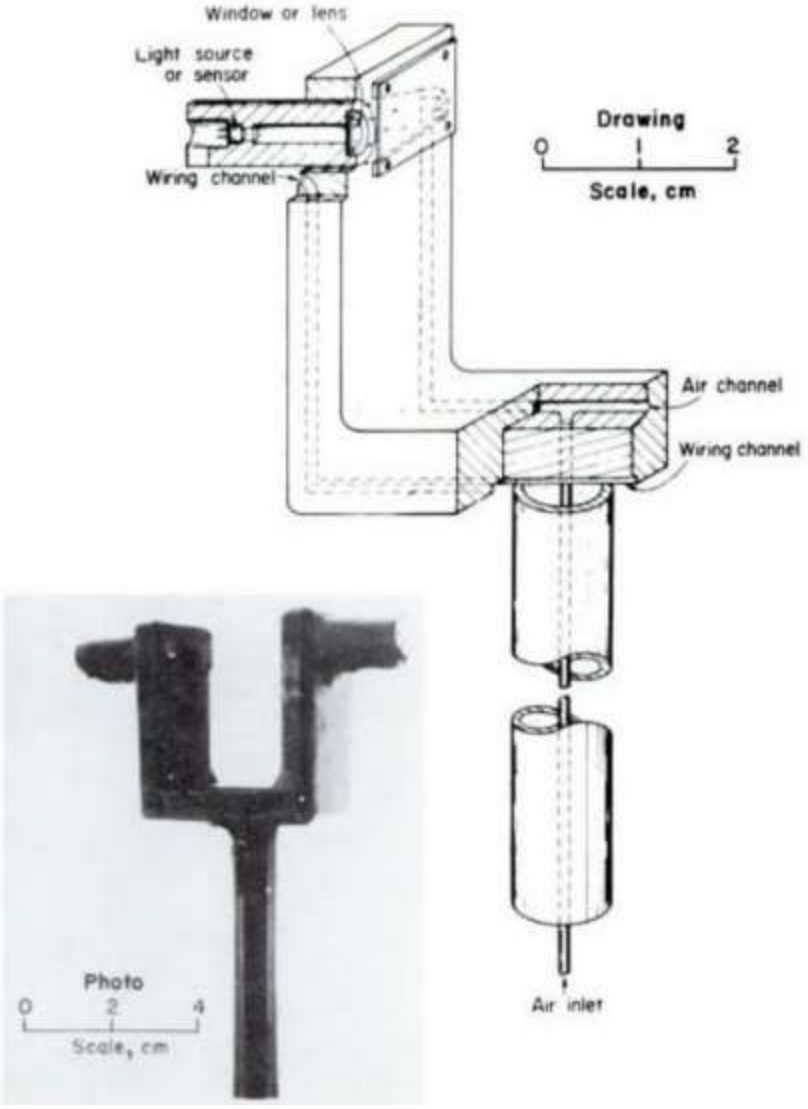

Figure 5-2. PRL's air jet dust probe system from the Three Probes study that prevented dust from accumulating on the lens covers.

A simpler, albeit untested, method of doing this would be to use specialized electrostatic dissipative (ESD) clear polycarbonate as consumable lens guards. It is unknown as to whether these could be used during an actual ANKO detonation (with the excess heat that occurs); however, in dry run testing they could serve the dual purpose of preventing dust accumulation and shielding the lenses from being sandblasted by the pressurized jet of abrasive powder.

5.3 Potential Application for Fines Characterization

An unexpected result from this research came from noticing that the tail end of the extinction coefficient curve for both the footage and probe data did not immediately return to zero after the cloud had passed.

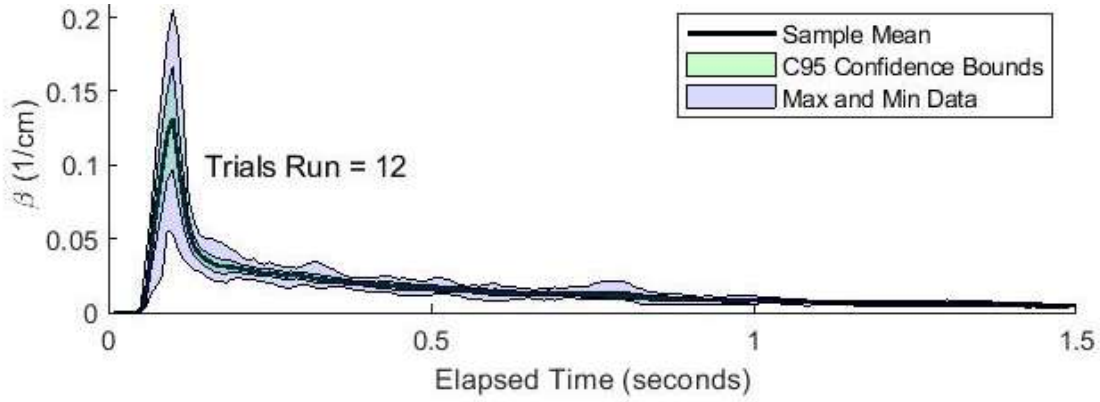

Figure 5-3. A time-extended version of the plot from Figure 4-1, showing how the probe data does not immediately return to a reading of zero after the cloud passes. This likely indicates the presence of fines.

Upon further inspection, it was deduced that this is largely the result of *fines*, or smaller particles that have been broken down, remaining suspended in the air long after the cloud has passed. This is a particularly interesting observation, as measuring and characterizing fines for a sample of AM powder is an active area of research at LLNL. Although further conclusions of this are beyond the scope of this thesis, there is certainly reason to suggest that the methods employed and detailed in this paper could be adapted and utilized in the realm of fines characterization for AM powders.

References

[1] K. Stevenson, "Understanding The Metal 3D Print Condensate Problem," Fabbaloo, 2021. [Online]. Available: https://www.fabbaloo.com/news/understanding-the-metal-3d-print-condensate-problem.

[2] "Metal 3D Printing: Who Needs Supports?," MachineDesign, [Online]. Available: https://www.machinedesign.com/3d-printing-cad/article/21154652/metal-3d-printing-who-needs-supports.

[3] ASTM International, "Standard Test Method for Explosibility of Dust Clouds".

[4] Ruwac, "DEADLY METAL DUST EXPLOSION IN CHINA SERVES AS A WARNING TO AMERICAN MANUFACTURERS, TOO," August 2014. [Online]. Available: https://www.ruwac.com/news/deadly-metal-dust-explosion-in-china-serves-as-a-warning-to-american-manufacturers-too/.

[5] "20-Liter Sphere Apparatus," ANKO, 2016. [Online]. Available: http://anko-lab.com/en/a/20-liter-sphere-apparatus. [Accessed 2021].

[6] S. J. Lampshire, "Metal Dust Cloud Distribution Characterization Through Image Analysis," California Polytechnic State University, San Luis Obispo, 2021.

[7] I. L. R. S. C. K.L. Cashdollar, "Three Bureau of Mines Optical Dust Probes," Pitsburgh Research Laboratory, 1981.

[8] K. L. Cashdollar, O. Kalejaiye, P. R. Amyotte and M. J. Pegg, "Effectiveness of dust dispersion in the 20-L Siwek chamber," *Journal of Loss Prevention in the Process Industries,* vol. 23, no. 1, pp. 46-59, 2010.

[9] BW TEK, "Spectrometer Knowledge," [Online]. Available: https://bwtek.com/spectrometer-part-8-fiber-optic-probes/.

[10] T. K. Takeshi Sato, "Field test of a new snow-particle counter (SPC) system," *Annals of Glaciology,* vol. 18, 1993.

[11] e. a. P. Gorner, "Photometer Measurement of Polydisperse Aerosols," Elsevier Science Ltd, 1995.

[12] W. C. Hinds, "Optical Properties," in *Aerosol Technology*, Wiley-Interscience, 1999, pp. 349-378.

[13] R. Nave, "Wave-Particle Dualtiy," Georgia State University, 2016. [Online]. Available: http://hyperphysics.phy-astr.gsu.edu/hbase/mod1.html.

[14] D. C. S. Baird, "Science Questions with Surprising Answers," West Texas A&M University, 2 July 2014. [Online]. Available: https://www.wtamu.edu/~cbaird/sq/2014/07/02/how-does-diffraction-make-a-trees-shadow-blurry/.

[15] R. A. Ogle, Dust Explosion Dynamics, Elsevier Science & Technology, 2016.

[16] R. K. A. Yumeng Zhao, "A real-time method for sensing suspended dust concentration from the light extinction coefficient," *Journal of Loss Prevention in the Process Industries,* no. 67, 2020.

[17] "Perfectly Spherical Tungsten Powder," Tekna, [Online]. Available: https://www.tekna.com/spherical-powders/tungsten.

[18] H.-J. O. D.-J. P. H.-C. H. C.-Y. G. T.-S. S. Hong-Chun Wu, "Dust Explosion Characteristics of Agglomerated 35 nm and 100 nm Aluminum Particles," *International Journal of Chemical Engineering,* vol. 2010, p. 6, 2010.

[19] J. Hecht, "Short history of laser development," SPIE, 1 September 2010. [Online]. Available: https://www.spiedigitallibrary.org/journals/optical-engineering/volume-49/issue-09/091002/Short-history-of-laser-development/10.1117/1.3483597.full?SSO=1.

[20] S. M. Goldwasser, " Diode Lasers - Why Can an LED Not be Focused Like a Laser Diode?," Sci.Electronics.Repair FAQ, 8 October 2005. [Online]. Available: http://repairfaq.cis.upenn.edu/sam/laserdio.htm#dioled.

[21] M. Rober, "Glitter Bomb 3.0," Youtube, 2020. [Online]. Available: https://www.youtube.com/watch?v=h4T_LlK1VE4.

[22] Thorlabs, "Power Meter Measurements," Thorlabs. [Online].

[23] D. Smith, "Calculating the Emission Spectra from Common Light Sources," COMSOL, 2016. [Online]. Available: https://www.comsol.com/blogs/calculating-the-emission-spectra-from-common-light-sources/.

[24] E. e. al., "A Comparison of Percieved and Measured Visibility in a Smoke Filled Corridor," 2017.

[25] T. N. Museum, "What is a CMOS image sensor?," [Online]. Available: https://www.tel.com/museum/exhibition/principle/cmos.html.

[26] American Meterological Society, "Pixel Value," 2012. [Online]. Available: https://glossary.ametsoc.org/wiki/Pixel_value.

[27] F. D. Devore, Applied Statistics for Engineers and Scientists, CENGAGE Learning, 2013.

[28] F. Wang and A. Theuwissen, "Linearity analysis of a CMOS image sensor," Society for Imaging Science and Technology, 2017.

[29] H. H. N. V. Peter Massingberd-Mundy, "A Practical Method for Testing Smoke Detectors With Drift Compensation on Slowly Developing Fires and High Background Levels," IFSEC Global.

[30] E. Fundamentals, "Laser Cutting," [Online]. Available: https://www.efunda.com/processes/metal_processing/laser_cutting.cfm#:~:text=Laser%20cutting%20machines%20can%20accurately,to%20the%20CNC%2FTurret%20process..

[31] W. E. Frazier, "Metal Additive Manufacturing: A Review," *Journal of Materials Engineering and Performance,* vol. 23, 2014.

[32] B. Du, W. Huang, L. Liu, T. Zhang, H. Li, Y. Ren and H. Wang, "Visualization and analysis of dispersion process of combustible dust in a transparent Siwek 20-L chamber," *Journal of Loss Prevention in the Process Industries,* vol. 33, pp. 213-221, 2015.

[33] N. S. Reding and M. B. Shiflett, "Metal Dust Explosion Hazards: A Technical Review," *Industrial & Engineering Chemistry Research,* vol. 57, pp. 11473-11482, 2018.

[34] "Combustible Dust Hazard Study," U.S. Chemical Safety and Hazard Investigation Board, 2006.

[35] K. L. Cashdollar, "Overview of dust explosibility characteristics," *Journal of Loss Prevention in the Process Industries,* vol. 13, no. 3-5, pp. 183-199, 2000.

[36] C. C. f. R. Sensing, "Fundamentals of Remote Sensing," Canada Centre for Mapping and Earth Observation, 2019.

[37] "The Electromagnetic Spectrum," NASA, March 2013. [Online]. Available: https://imagine.gsfc.nasa.gov/science/toolbox/emspectrum1.html#:~:text=Radio%20waves%2C%20gamma%2Drays%2C,electromagnetic%20spectrum%20are%20electromagnetic%20radiation..

[38] OpenStax, "Nature of Light," in *University Physics*.

[39] S. C. M. A. M. R. a. S. S. Q. C. D. Boley, "Metal powder absorptivity: modeling and experiment," *Applied Optics,* 2016.

[40] I.-M. e. al., "Sphericity and roundness computation for particles using the extreme vertices model," *Journal of Computational Science ,* 2018.

Appendix

A.1 Issues with using a Smart Phone Camera

As discussed in section 5.1.1, the highspeed camera was difficult to get viable data with. Limited to a low frame rate of 120 fps due to the AC backlight, switching to an iPhone 6s for slow motion footage seemed to be a much more efficient option than the highspeed camera. Unfortunately, after analyzing some trials of iPhone footage in MATLAB, it was observed that some auto-adjustments were occurring over the course of the trial, despite the use of the iPhone's Auto Exposure/Auto Focus (AE/AF) Lock. This was an important discovery, as any auto-adjustments could skew the pixel intensity measurements gained from the footage. This observation led to the development of the camera calibration process detailed in section 3.3.2, which was completed on the iPhone 6s default camera app with the AE/AF Lock activated.

Figure A-1. Still shots extracted from iPhone footage for use in the camera calibration process.

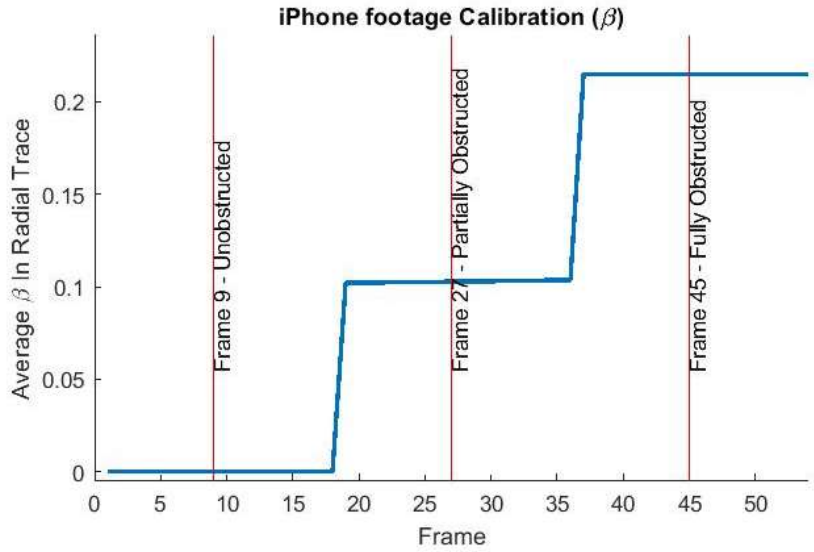

Figure A-2. Average extinction coefficient for iPhone 6s camera calibration.

As can be seen in the figure above, the AE/AF Lock was ineffective at locking out any auto-adjustments occurring in the camera. Upon further investigation, it was determined that the camera was designed to make fine-tuned adjustments to achieve the ideal picture warmth and temperature, otherwise known as an Auto-adjust White Balance (AWB) function. There was no apparent method to turn AWB off on the default camera app for the iPhone 6s. To still enable the usage of the iPhone 6s camera for slow motion video, an auxiliary camera app, CameraPro, which was purported to offer the user full manual control over the phone's camera (including AWB locking), was downloaded for testing.

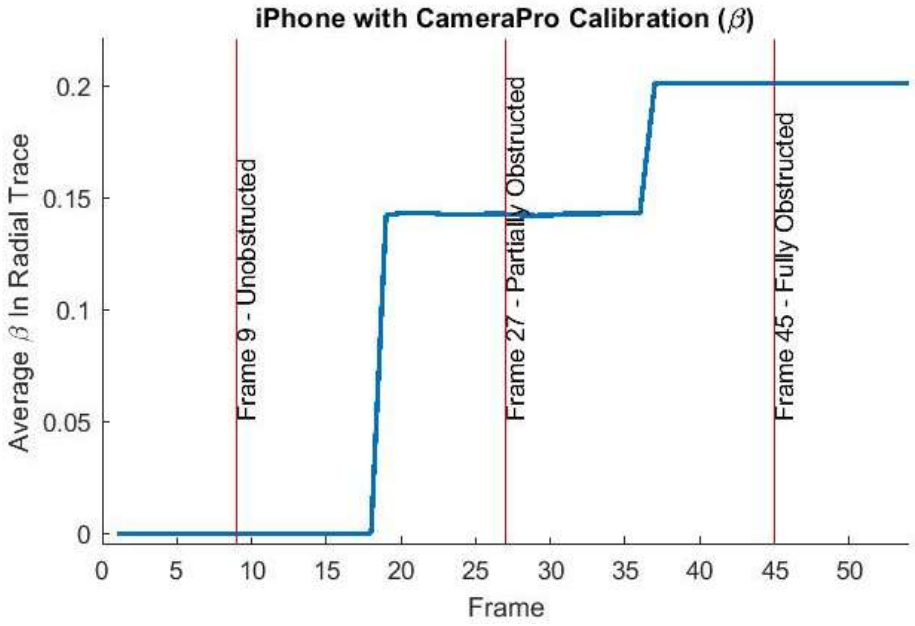

Figure A-3. Average extinction coefficient for iPhone 6s camera calibration with CameraPro app.

Surprisingly, there were still small auto-adjustment effects occurring when using CameraPro in manual mode. Although the degree of auto adjustment was significantly less for footage taken with CameraPro than with the default iPhone camera app, the conclusion from this finding was that the iPhone 6s was not a viable option as a camera for this experiment. This finding highlights the importance of the footage calibration process with digital cameras.

A.2 Study in Probe Extinction Coefficient vs Mass of Powder Sample

Although the camera setup was limited to a sample collection rate of only 120Hz due to the AC backlight, as discussed in section 3.1.4, the probes could take data at a much higher rate without being affected by this AC strobe effect. Consequently, a separate set of trials with the probes taking data at a higher sampling rate of 480 Hz was conducted without the highspeed camera. Omitting the highspeed camera greatly expedited data collection and enabled a separate set of 30 total trials to be taken with just the probe, at 10 trials each for 3 different amounts of powder: 20g, 40g, and 60g.

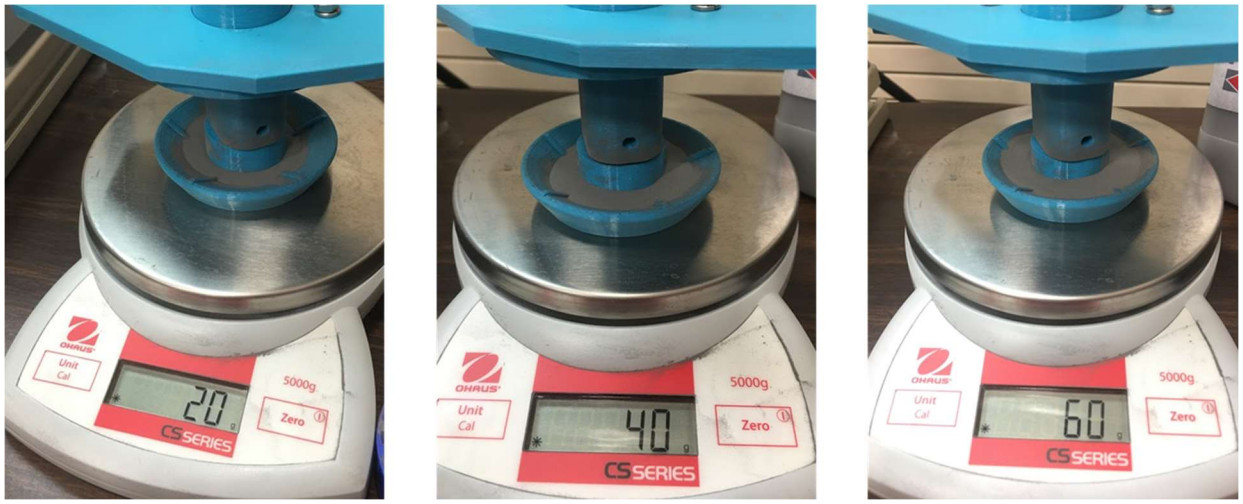

Figure A-4. Different amounts of powder in probe trials: 20g, 40g, and 60g.

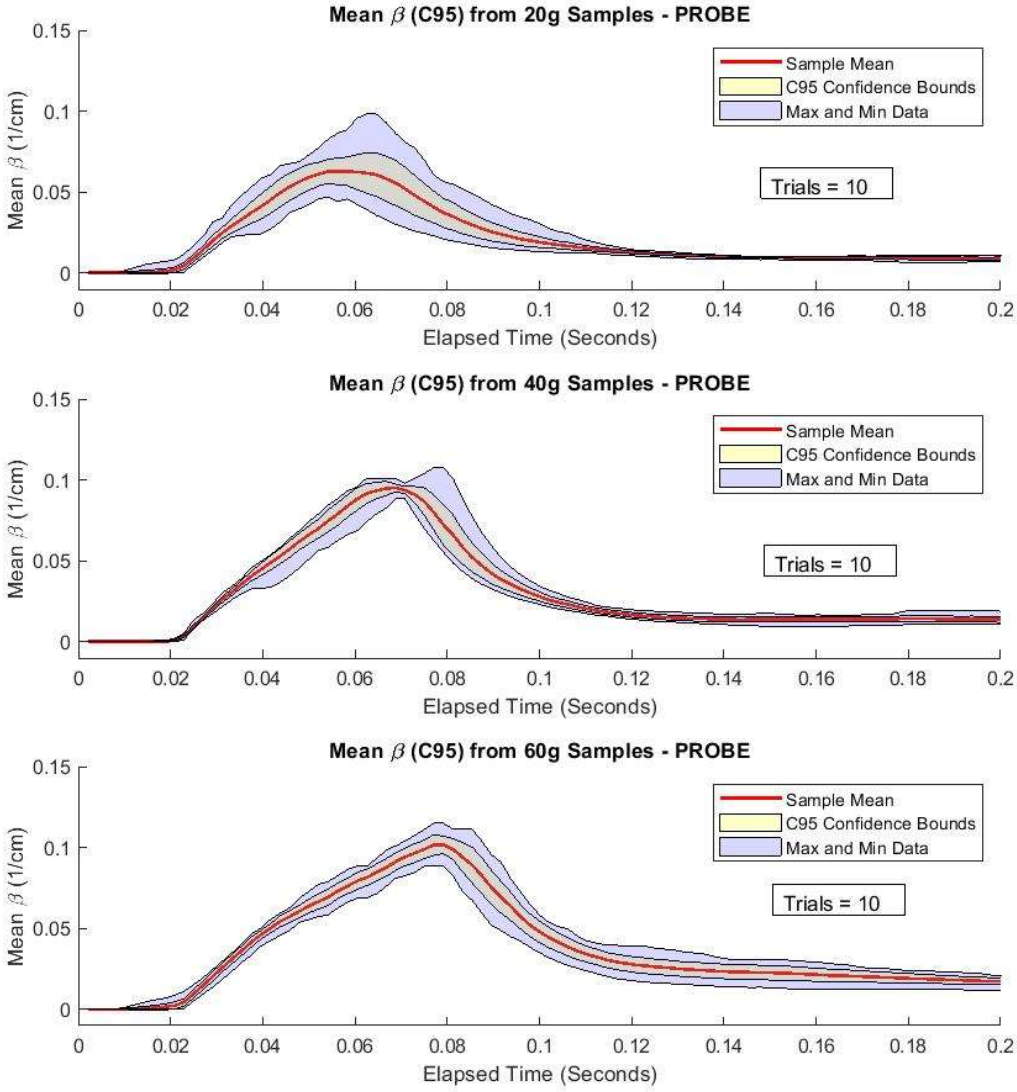

Figure A-5. Mean extinction coefficient, 95% confidence interval (C95), and data bounds over time for 20g, 40g, and 60g samples. Each sample had 10 trials, recorded at 480 Hz.

Due to this extra data collection being outside of the scope of the thesis, further numerical analysis was not completed beyond producing the plots shown above. Qualitatively, it appeared that the general spread of the data narrowed for the test setup as the mass of the powder increased, alluding to the mass of the powder sample having an effect on the repeatability of the setup.

An interesting observation was that the spread of the probe data for 40g trials taken at 120 Hz, shown back in Figure 4-9, was significantly larger than the spread of the data for the 40g trials taken at 480 Hz, shown above. This highlights both the necessity for both better time resolution in data collection, larger sample sizes, and outlier analysis in data processing.

A.3 Cal Poly Powder Safety Testing Plan

** Note: This appendix document may not match the formatting of the rest of the thesis **

Process

Create a tungsten metal powder cloud in a testing enclosure.

Purpose

During the period of Fall, Winter, and Spring quarter of 2020/2021, Shelby Lampshire and Spencer Grenley will be completing a series of tests to generate data for their master's thesis. The testing goal is to replicate a tungsten powder dust cloud in a transparent, sealed enclosure in order to get high speed footage and optical density probe measurements.

Testing Enclosure Design

The testing enclosure includes a transparent cylinder with a top and bottom attached to a t-slot frame sitting on a table. At the top of the cylinder, a suspended testing sieve would hold tungsten metal powder. A mechanism will release the powder while inside the sealed enclosure. This will cause the powder to fall through the sieve and create a cloud. The drop test design is shown in the figure below.

Figure 1. Testing enclosure.

During testing, both top and bottom of the enclosure will be sealed to keep any dust from entering the surroundings. The bottom includes a collection pan for the powder to fall into that is held up against the bottom of the cylinder by the frame. When testing is finished and the powder has settled, the frame can be loosened to allow the pan to lower and the powder to be put back into its storage container.

The top of the cylinder is sealed with a flange, rubber ring, and acrylic plate sandwiched and clamped together.

Work Area

The area that has been approved for work on these theses is at Cal Poly in 13-126. No other people will be working in this lab during Fall and Winter quarter.

Figure 2. Lab space in 13-126 with rolling dock door accessible.

Materials and Set Up

The set up for the test will include a sealed transparent enclosure that will contain the metal powder cloud created during testing. This will sit on a flat surface along with a lighting set up and a nearby high-speed camera set up.

The material intended for the test is tungsten metal powder with a particle size averaging 38 μm in diameter. The powder is intended to be kept dry and sealed for the duration of testing. Approximately 2 kg of this tungsten powder will be supplied by Lawrence Livermore National Laboratory (LLNL) for testing purposes.

Metal Powder Handling and Storage

Any handling of metal powder will be done in a well-ventilated space with proper PPE. (See risk mitigation section below)

The proper storage of tungsten powder will be followed according to Lawrence Livermore National Lab's procedures. This will be available for this project soon.

Test Procedure:

1. Open rolling door to allow ventilation in the testing space.
2. Make sure enclosure is clean and sealed at the bottom with its collection system in place.
3. Take off top seal of enclosure and assemble the test sieve to fasteners, grounded wire, and motion arm.
4. Set up camera.

5. Make sure all PPE is on.
6. Take out powder from container and weigh amount needed for test (TBD how much powder)
7. Transfer powder into testing sieve as evenly as possible (some may drop through which is to be expected) Do not shake sieve.
8. Seal top of enclosure.
9. Close rolling door to eliminate outside light for glare.
10. Set up lighting and exposure and start camera
11. Perform test: shake outside arm to allow sieve to let the metal powder fall through until empty.
12. Stop camera filming.
13. Open rolling door.
14. Allow dust to entirely settle inside enclosure- maybe 15 minutes
15. Unseal the bottom collection system and carefully pour powder into storage container and seal.
16. Follow cleaning procedure.

Cleaning Procedure

After any handling of powder, all surfaces will be wiped down with wet wipes (in accordance with LLNL's recommendations). The wipes will be collected and stored until proper discarding.

The sealed collection system at the bottom of the enclosure will collect the bulk of the tungsten powder after the test. Once carefully emptied into the storage container, the interior cylinder walls will be wiped down to collect any leftover powder.

In the case of powder spillage, an antistatic broom will be used to collect the powder and it will be placed in a separate sealed container to be discarded properly.

Waste Disposal

The tungsten powder will be reused for testing, so minimal powder waste should be generated. However, all wipes and used disposable cleaning supplies will be collected and stored safely until a proper disposal processes can be completed. (See risk mitigation section below)

Risk Mitigation

Explosivity Risk: This powder has been tested for explosivity and has **not** been found to be explosive in the form (dry and with stated particle size) stated in the test. On attached Fike Document, see Appendix B, page 5 for reference.

However, the following procedures have been developed to mitigate even the slight risk of flammability or explosivity:

-The powder and testing setup will not be near any ignition or open flame

-The interior surfaces of the transparent enclosure will be coated with Licron Crystal™ Permanent Clear Static Dissipative coating to prevent static buildup during testing. This will not only decrease the dust cloud's tendency to line the surface of the enclosure but also mitigate the risk of any static charge buildup that could cause a spark or ignition during testing.

-The metal sieve has the capability to generate a static charge so we will connect it to a grounding wire to dissipate any charge

Toxicity Risk: The main risk of metal powder handling seems to come from skin to powder contact or inhalation. To mitigate these risks are the follow procedures:

- During any handling of uncontained metal powder, the following PPE will be worn by those in the room:

-Nitrile or chemical resistant gloves

-skin protective clothing (long pants, sleeves or lab coat, closed shoes)

-face shield or safety glasses

-respirator (particulate mask)

-The NIOSH-approved particulate filtering facepiece respirators started with N95 masks and increased in filtration from there, but due to the difficulty of acquiring those masks (Covid) we may have to use KN95 or similar.

-However, according to the CDC website, "Respirators should only be used when engineering control systems (such as adequate ventilation or scrubbing of contaminants) are not feasible. Engineering control systems are the preferred control methods for reducing worker exposures."

- When handling any uncontained metal powder, the large rolling dock door next to our working area will be open to allow adequate ventilation.

- After powder handling, all surfaces and tools will be wiped down to remove any contaminants.

Environmental Hazard Risk:

-The powder will be reused during testing so minimal waste will be produced

-However, a plan for a one-time waste disposal process at the end of testing will need to be developed.

-The environmental safety coordinator at LLNL has been contacted regarding this project. Their response will likely shape the waste disposal procedure.

A.4 Wiring Schematic for Probe

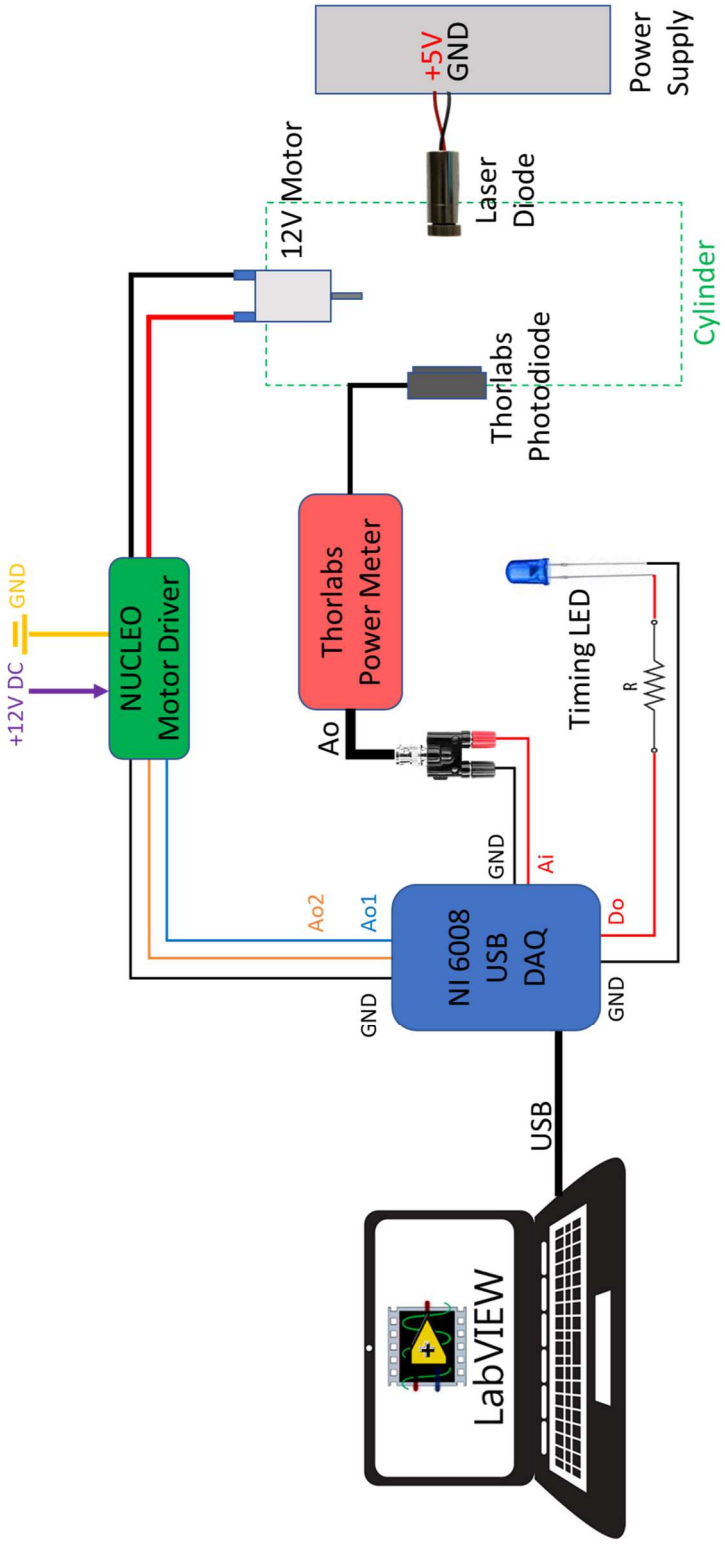

A.5 Dust Explosibility Metrics

In a dust explosibility test, the following values are found to determine the risk of accidental deflagration for a powder.

Property	Definition	ASTM Test Method	Application
K_{St}	Dust deflagration index	ASTM E 1226	Measures the relative explosion severity compared to other dusts.
P_{max}	Maximum explosion overpressure generated in the test chamber	ASTM E 1226	Used to design enclosures and predict the severity of the consequence.
$(dp/dt)_{max}$	Maximum rate of pressure rise	ASTM E 1226	Predicts the violence of an explosion. Used to calculate K_{St}.
MIE	Minimum Ignition energy	ASTM E 2019	Predicts the ease and likelihood of ignition of a dispersed dust cloud.
MEC	Minimum explosible concentration	ASTM E 1515	Measures the minimum amount of dust, dispersed in air, required to spread an explosion. Analogous to the lower flammability limit (LFL) for gas/air mixtures.
LOC	Limiting oxygen concentration	ASTM standard under development	Determines the least amount of oxygen required for explosion propagation through the dust cloud.
ECT	Electrostatic charging tendency	No ASTM standard	Predicts the likelihood of the material to develop and discharge sufficient static electricity to ignite a dispersed dust cloud.

A.6 How a 3D Concentration can be Derived from a Point Source

During this research, the question arose of how to calculate a measurement of three-dimensional mass concentration, in grams per cubic centimeters, from a one-dimensional point source method utilizing a laser beam. In part, the answer is that the laser is not truly a point source. When sufficiently collimated, it can be approximated as a column of light with a large diameter relative to the size of the particles. This cylindrical beam encompasses many particles in its volume.

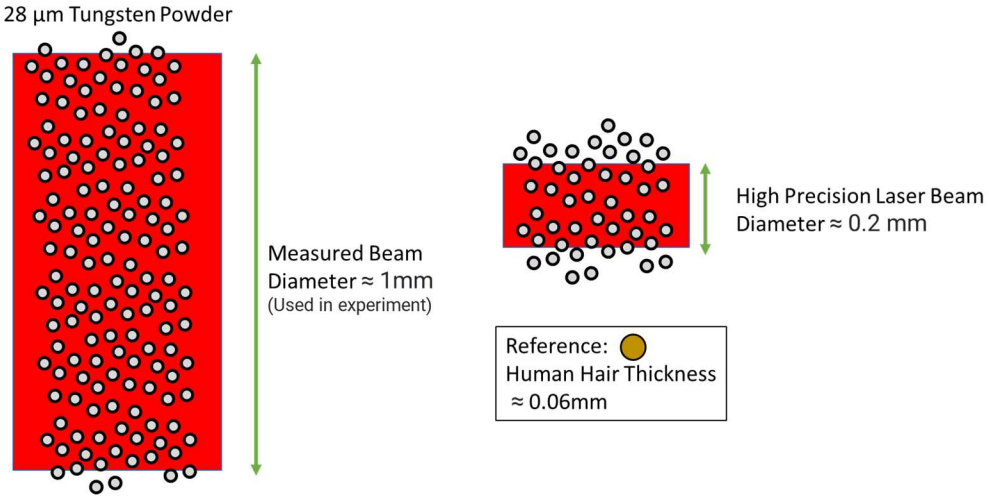

Figure A-6. Scale of laser beam diameter compared to particle size, illustrating what a high precision laser beam diameter would be compared to the inexpensive laser diode used in this experiment.

It is important to note that this measured beam diameter is a very rough estimate, completed with digital calipers. Additionally, the laser diode used was inexpensive and unfocused – for reference, the laser beam on an industrial laser cutter is about 0.2mm in diameter when properly adjusted [30].

A.7 Probe Calibration LabVIEW program

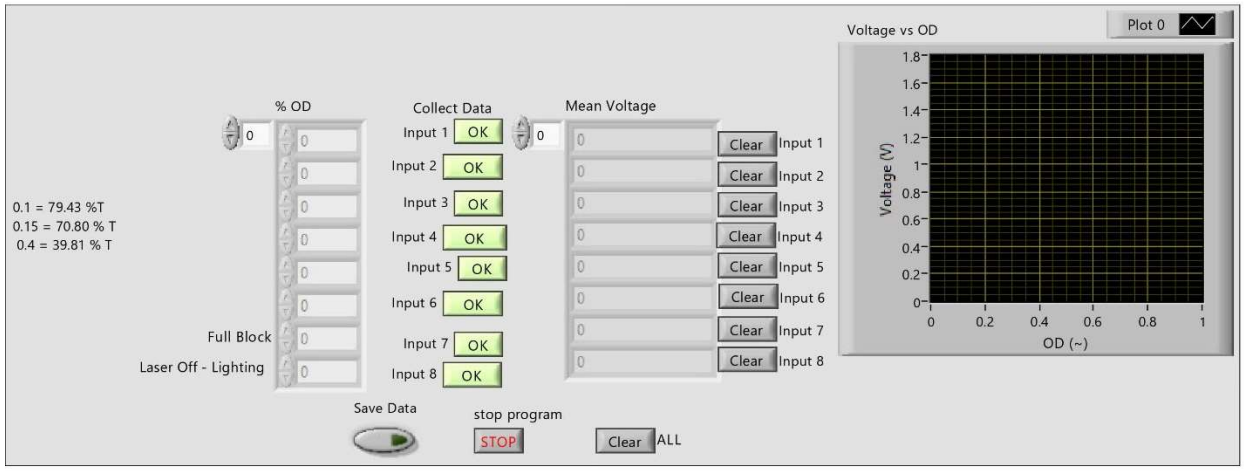

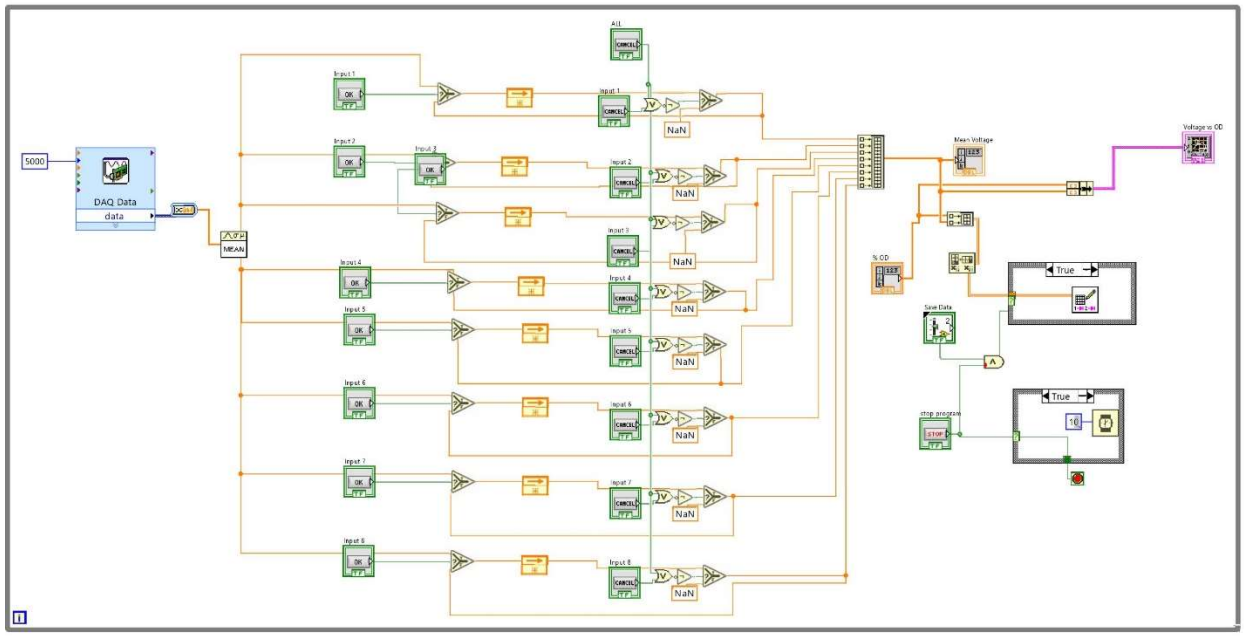

A.8 Data Collection LabVIEW program

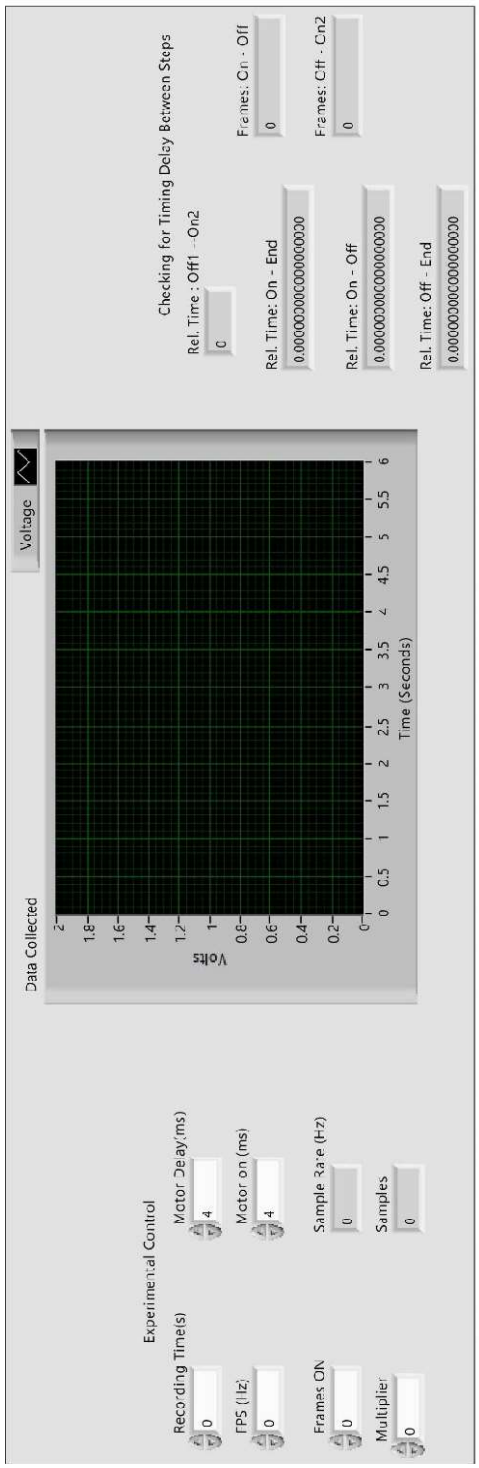

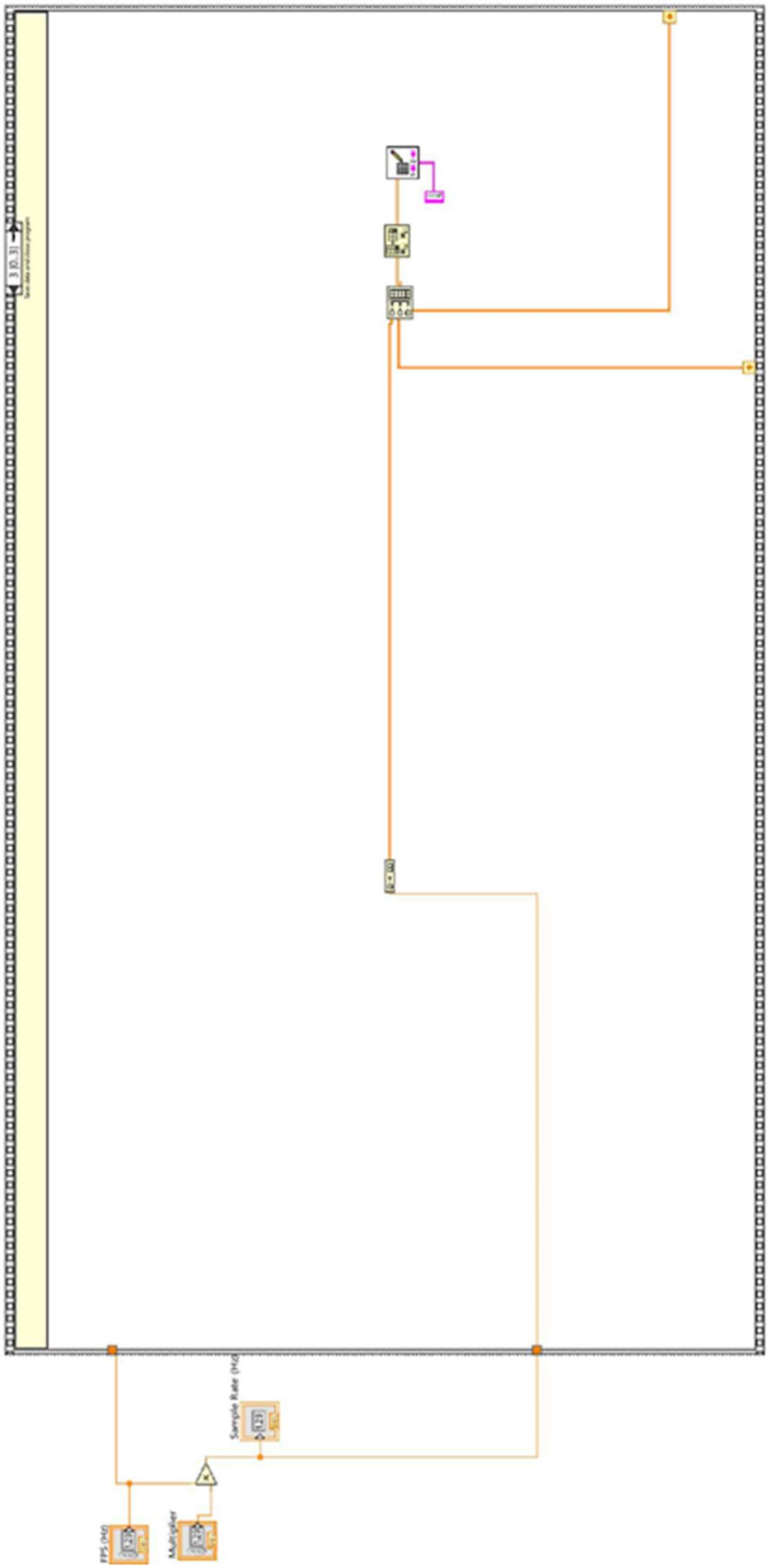
Sample Rate (Hz)
FPS (Hz)
Multiplier

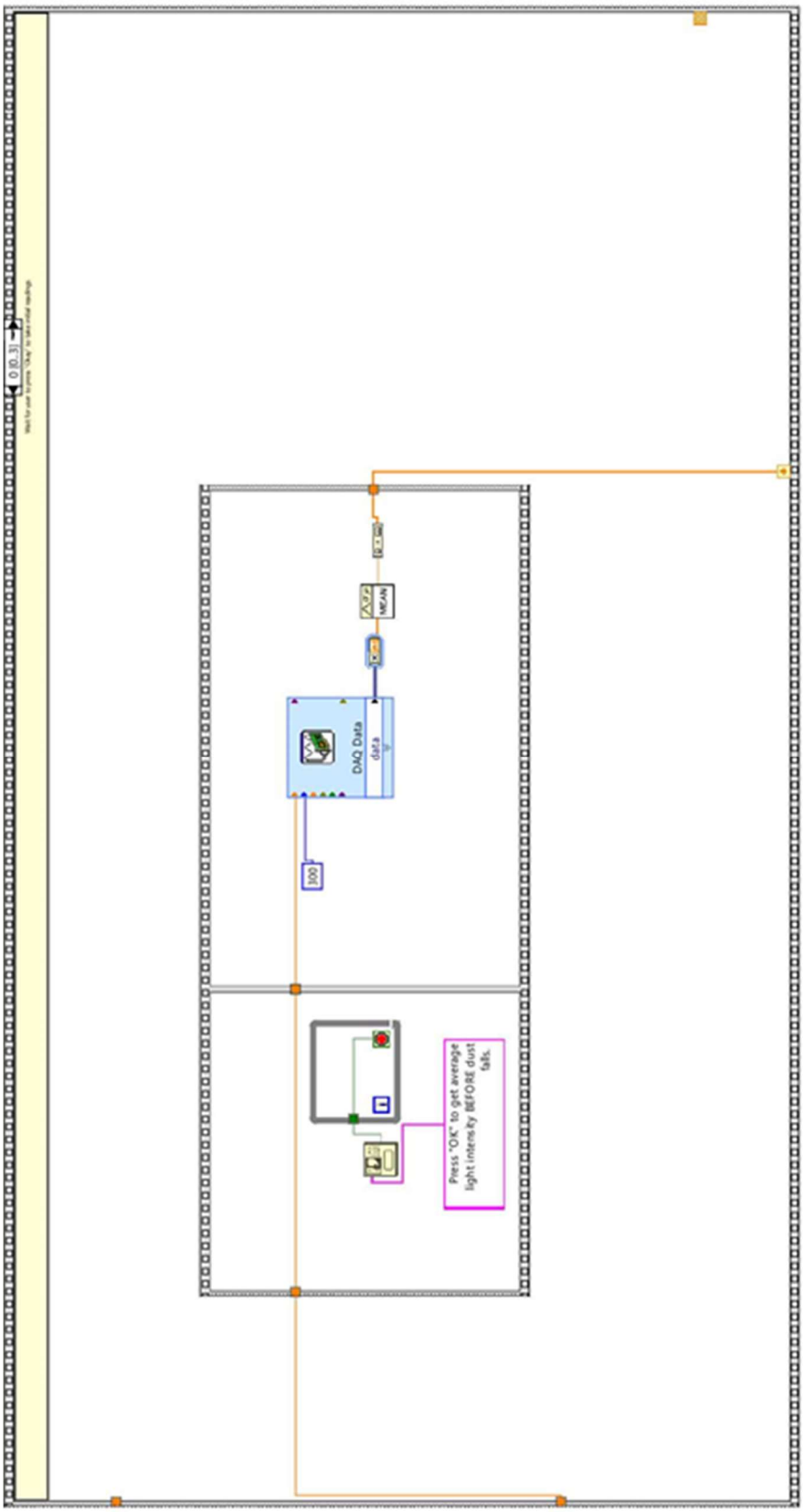
0 [0..3]
MEAN
DAQ Data
data
100
Press "OK" to get average light intensity BEFORE dust falls.

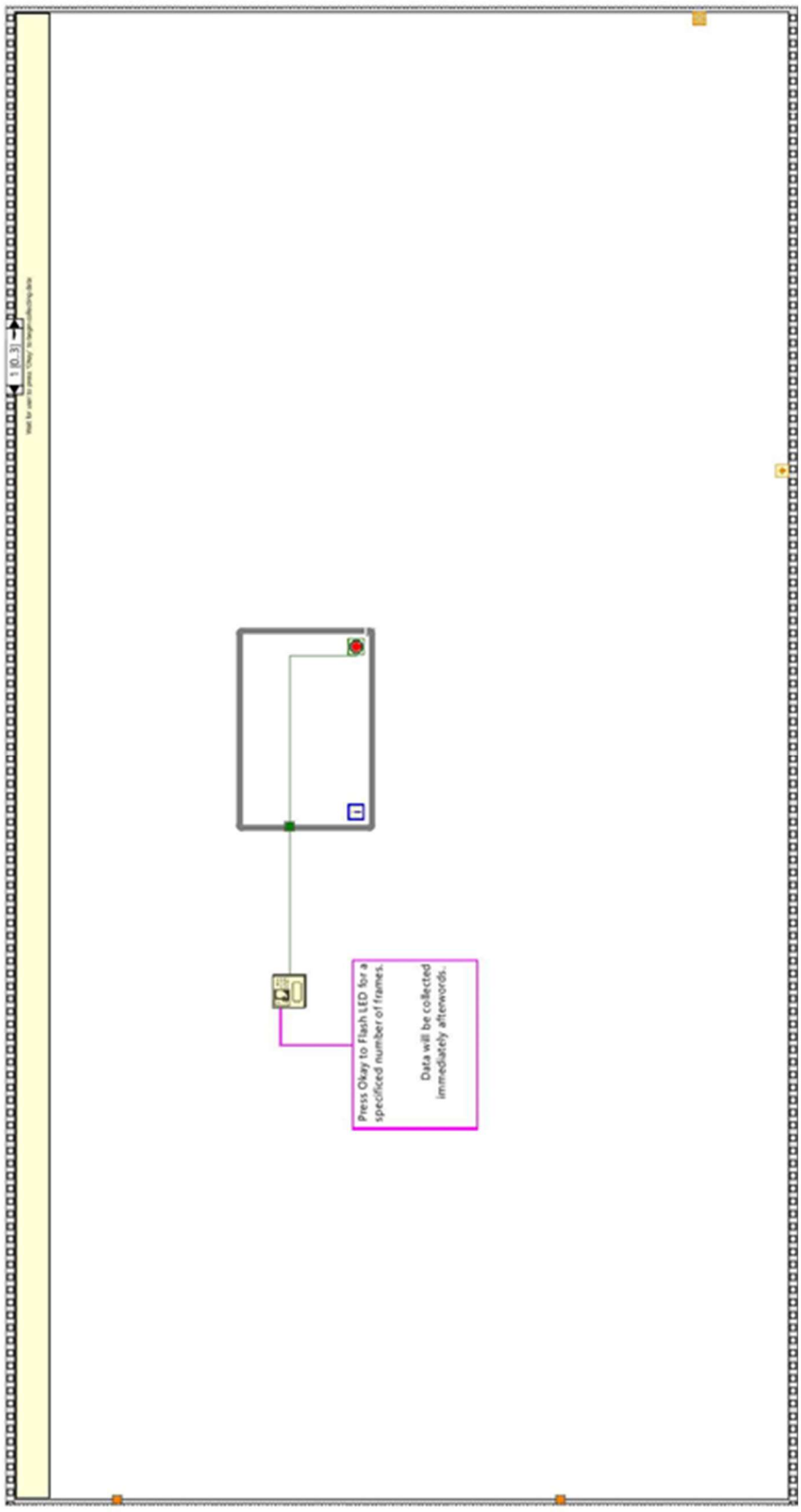
i [0..3]
Press Okay to Flash LED for a specificed number of frames.
Data will be collected immediately afterwards.

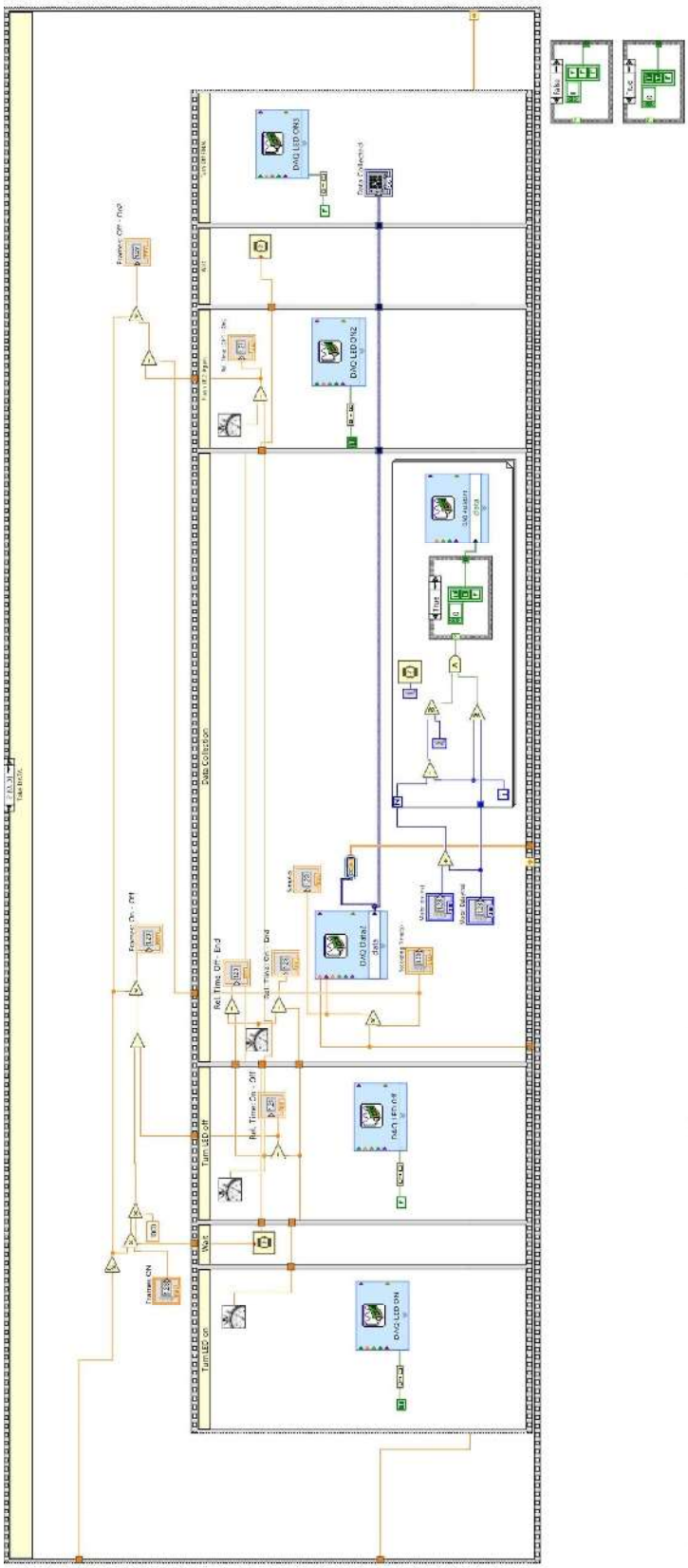
Data Collection
Turn LED on
Wait
Turn LED off
DAQ LED ON3
DAQ LED ON2
DAQ LED ON1
DAQ LED OFF
DAQ Digital
Wait
Rel. Time On - End
Rel. Time On - Off
Rel. Time Off - End
Rel. Time Off - On
Frames On - Off
Frames Off - On
Frames ON
Status
Data Collected

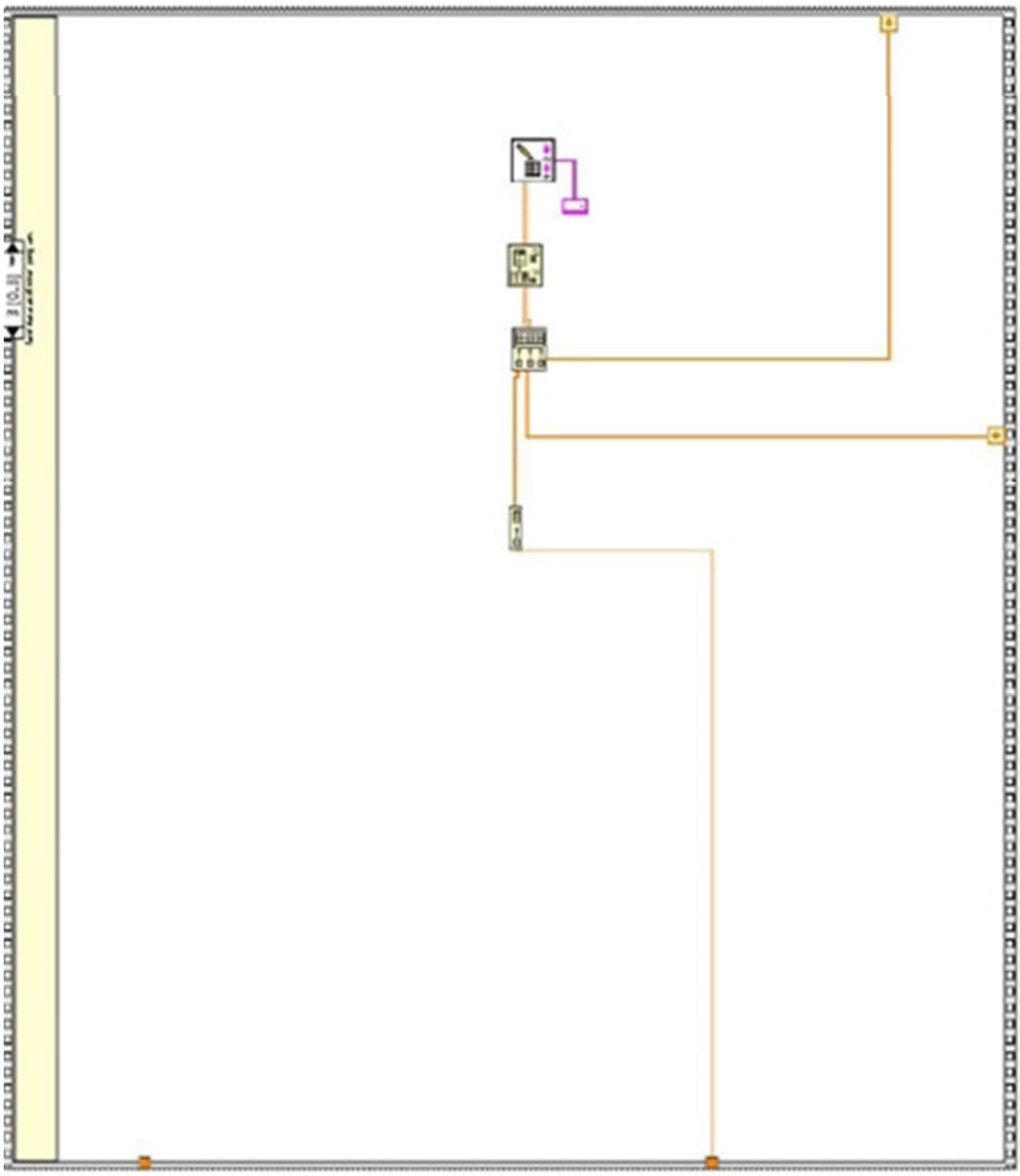

A.9 Calculations for Sufficiently Removed Distance

Below are the detailed calculations for Eqn. (8) and Eqn. (9).

Objective: Extrapolate an equation to approximate the sufficiently removed distance for a detector for the extinction paradox to occur (Using information from Hinds)

Inputs:

$d_p := 28\ \mu m$	Particle diameter
$\lambda := 650\ nm$	Wavelength of light for circular sensor
$A_s := 75\ mm^2$	Active area of sensor (if circular)
$h_s := 5\ mm$	Height of active area (if rectangular)

Extinction Paradox [Hinds]

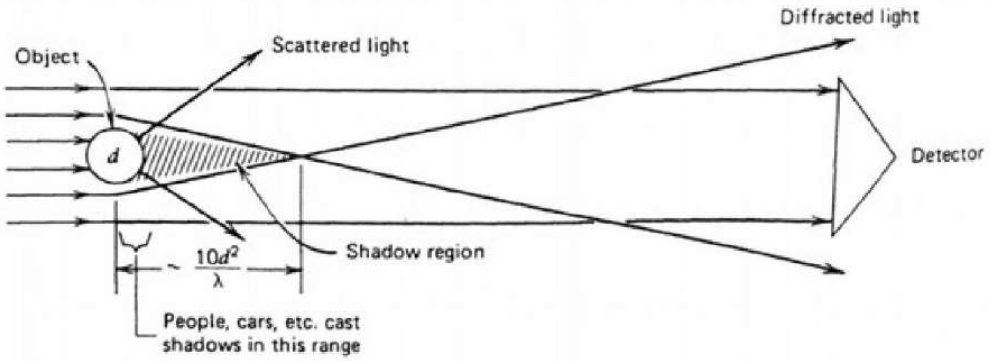

FIGURE 16.4 Diagram of extinction paradox.

Simplified Image

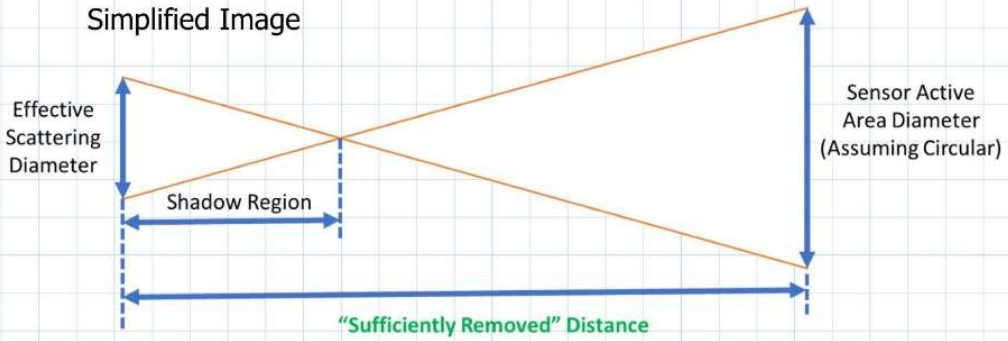

The Effective Scattering Diameter is a contrived concept for the purpose of this calculation. It is based on the notion that, when Q = 2 during the extinction paradox, the light is effectively blocked by a factor of 2. This implies that the effective area of the particle is twice as large as its actual projected area. The effective scattering diameter is simply double that of the actual diameter of the particle.

Assumption: Effective scattering area = double projected area

$d_{eff} := \sqrt{2}\ d_p = 39.598\ \mu m$ Effective scattering diameter

$d_s := \sqrt{\frac{4}{\pi} \cdot A_s} = 0.977\ cm$ Diameter of sensor active area

$L_{shadow} := \frac{10 \cdot d_p^{\ 2}}{\lambda} = 1.206\ cm$ Length of shadow region [Hinds]

Output:

Sufficiently removed distance (for circular active area)

$$L_{suf.circ} := L_{shadow} + L_{shadow} \cdot \frac{d_s}{d_{eff}}$$

$$L_{suf.circ} = 2.989\ m$$

Conservative (without using effective scattering diameter)

$$L_{suf.circ.consv} := L_{shadow} + L_{shadow} \cdot \frac{d_s}{d_p}$$

$$L_{suf.circ.consv} = 4.222\ m$$

$$scalar_{circ} := \frac{L_{suf.circ.consv}}{L_{suf.circ}} = 1.413$$

Sufficiently removed distance (for rectangular active area)

$$L_{suf.rect} := L_{shadow} + L_{shadow} \cdot \frac{h_s}{d_{eff}}$$

$$L_{suf.rect} = 1.535\ m$$

Conservative (without using effective scattering diameter)

$$L_{suf.rect.consv} := L_{shadow} + L_{shadow} \cdot \frac{h_s}{d_p}$$

$$L_{suf.rect.consv} = 2.166\ m$$

$$scalar_{rect} := \frac{L_{suf.rect.consv}}{L_{suf.rect}} = 1.411$$

Equation in variable form

$$L_{suf} := \frac{10\ {d_p}^2 + 5\ \sqrt{2} \cdot d_p \cdot d_s}{\lambda} = 2.989\ m$$

A.10 Time Discrepancy from Radial Trace Placement

In the image analysis post-processing of all trials, the center of the radial trace was placed approximately 10 pixels above the laser beam line.

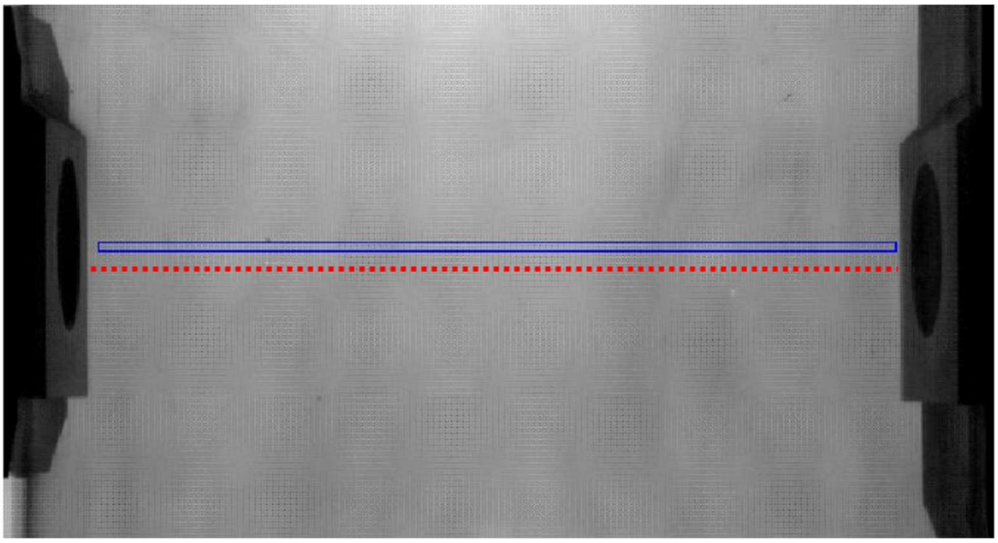

The approximate speed that the powder cloud fell was determined by measuring how many pixels the edge of one of the plumes traveled between two frames. This distance, combined with the known elapsed time between frames of 1/120 seconds, produced the approximate powder cloud velocity of 8880 pixels/second. Using the speed of the powder cloud along with the known pixel height offset of 10 pixels, the time offset was approximated:

$$\text{Time Offset} = \frac{10 \text{ pixels}}{8880 \text{ pixels/second}} = 1.13 \text{ ms}$$

The timing error of 1.13 ms produced by the vertical offset between the radial trace and laser beam was determined to be negligible relative to the total time duration of the trial, which was stated to be 100 ms in section 4.2.